Generic and broadband non-linear time domain impedance boundary condition

Rémi Roncen, José Cardesa

To cite this version:

Rémi Roncen, José Cardesa. Generic and broadband non-linear time domain impedance boundary condition. Journal of Sound and Vibration, 2023, 554, pp.117691. 10.1016/j.jsv.2023.117691 . hal-03889552v2

HAL Id: hal-03889552

https://hal.science/hal-03889552v2

Submitted on 7 Apr 2023

Generic and broadband non-linear time domain impedance boundary condition

Rémi Roncen *[1] and José Cardesa[1]

[1]ONERA/Département Multi-Physique pour l'Énergétique, Université de Toulouse, F-31055, Toulouse, France

Abstract

An approach for modeling time-domain impedance boundary conditions (TDIBC) is presented. Its implementation in numerical codes relies on the inverse Fourier transform to recast the convolution problem into an array rolling operation. The proposed approach offers several advantages, including an inherently broadband formulation that can handle discontinuous waves, the ability to cater for any impedance law on frequency, ease of extension to non-linear impedance operators, and the elimination of ad-hoc, previously-tuned parameters. The linear solver, whose code is shared, is first validated against theoretical results. The non-linear solver is then validated against experimental data obtained in an impedance tube setting. Finally, a fully non-linear Navier-Stokes solver based on discontinuous spectral differences is utilized to demonstrate the implementation of the TDIBC in a grazing incidence duct configuration.

Keywords: impedance, scattering, direct convolution, dynamic impulse response, TDIBC, broadband, non-linear, discontinuous, spectral difference

1 Introduction

In the field of aeroacoustics, passive wall treatments called liners are used in engine nacelles to suppress noise propagation [1]. These materials are most commonly made of assemblies of perforated sheets bonded onto honeycomb cavities, and operate on the principle of resonators [2, 3]. The fundamental characteristic of these materials is the surface impedance, which in the frequency domain establishes a transfer function between the acoustic pressure and the acoustic particle velocity normal to the liner [4]. If the acoustic behavior of the material is independent of the incident wave direction, then the liner is considered to be locally-reacting, and the surface impedance becomes the defining property (Ref. [5] provides a guide for the measurement of impedance on non-locally reactive samples). Another field of interest for impedance boundary conditions (IBCs) is the study of combustion chambers, where liners can be used to reduce thermoacoustic instabilities [6–8]. In such scenarios, IBCs provide a convenient tool to replace some element of the geometry within a large-eddy simulation, allowing the simulation domain to be truncated. The implementation of an IBC in computational studies was shown to significantly reduce the numerical cost of the simulation while preserving the critical acoustic features that drive the system instabilities [9]. Due to the many analogies between the acoustic and electromagnetic computational problems, the development of IBCs has been concurrently explored in both fields of research. The present study focuses on (aero)-acoustic problems, but is a-priori not restricted to them.

Although the impedance modeling of acoustic liners was initially conducted in the frequency domain, most aeroacoustic codes rely on solving time-domain equations. This approach is highly suitable for computational aeroacoustics (CAA), as it allows considering non-linear problems governed by the Euler or Navier-Stokes equations. Additionally, in the presence of a high sound pressure level (SPL), non-linear phenomena can occur in the vicinity of the liner perforations [10, 11], thereby complicating the impedance modeling in the frequency domain. Other advantages of a time-domain representation include the capacity to process sound signals with a broad frequency spectrum and moving sources.

In recent decades, there has been significant progress in the development of impedance models in the time domain, which have demonstrated their ability to target broadband behaviors and to handle non-linear impedance operators [12]. The majority of these techniques rely on approximating the complex, frequency-dependent impedance operator with rational functions, and are separated in three families: recursive convolution, z-transform and auxiliary differential equations (ADE). Further elaboration on each family is provided below.

---

*Corresponding author: remi.roncen@onera.fr

Recursive convolution approach Yee [13] pioneered the field of research on the finite-difference time-domain (FDTD) approach to solving Maxwell's equations with constant values of the permittivity and conductivity of materials (equivalent to constant impedance). This enabled narrow-band time-domain simulations. Building upon the FDTD approach of Yee, Luebbers et al. [14] introduced the first family of solutions to the frequency-dependent problem by approximating the convolution with an operator (similar to the impedance) via a time discretization technique. Arbitrary order polynomial approximations of the operator were considered, thus extending the initial work of Luebbers et al. in Ref. [15]. By assuming a linear change in variables over time, the complex time-domain convolution was reduced to a recursive algorithm. In the field of acoustics, recursive methods were introduced by Reymen et al. [16], who efficiently implemented the time-domain boundary condition developed by Tam and Auriautt [17].

z-transform approach Özyörük et al. [18] were the first to explore time-domain solutions to an aeroacoustic problem based on an impedance-modeled liner assuming a linear response. The authors recognized that the direct convolution of the impedance operator between the pressure and velocity fields could be accomplished recursively at each time step. To reduce memory requirements, the authors chose to rephrase the convolution problem using the z-transform. This z-transform strategy, which represents the impedance as a digital filter, had been used previously by Sullivan for the Maxwell equations within dispersive media featuring frequency-dependent properties [19, 20]. Combining the Myers approach to IBC modeling [21], Özyörük et al. approximated the real and imaginary parts of the impedance using rational polynomials whose coefficients served as degrees of freedom (DoF) of the time-domain impedance boundary condition (TDIBC). To ensure the stability and causality of the impedance, constraints were imposed on the roots and poles of these polynomials. These limitations were due to the lack of physical significance of the polynomial coefficients, which constrained the flexibility of the approach and the goodness of fit of the polynomials to the available data. To overcome this constraint and achieve a closer representation of the physics, Rienstra [22] proposed an alternative method where a single degree of freedom liner (SDoF) made up of a perforated sheet backed by a cavity, called the extended Helmholtz resonator (EHR) model, was represented using five parameters. The EHR model was shown in Ref. [12] to be a generalization of the $\lambda/4$ resonator model and Ko's model [23].

Auxiliary differential equations (ADE) approach Based on a recommendation made by Jackson [24, p. 331], Joseph et al. [25] used the FDTD approach with Maxwell's equations and examined the first and second order frequency dependencies of the dispersion operator. Using the inverse Fourier transform (iFT) of the dispersion operator, the authors proceeded to reframe the convolution problem using additional equations, thus pioneering the so called ADE approach. Subsequently, the ADE approach was demonstrated to maintain the order of accuracy of the time integration scheme, which was not the case for the recursive convolution methods that were limited to first and second order accuracy [26].

Starting from physically-sound acoustic impedance models in the frequency domain, Monteghetti et al. [27] introduced the oscillatory-diffusive (OD) approach to the TDIBC, which is a specific type of ADE that makes use of delayed ordinary differential equations. The OD-TDIBC consists in recasting the convolution problem using a sum of first order polynomials representing an operator, such as the scattering or the impedance. With the adoption of the OD representation, a set of additional variables extends the system, and auxiliary equations on these parameters must be solved along with the initial ones. A first advantage of the OD-TDIBC approach is that physical guidelines were given to choose some of the model's DoFs, while the remainder could be obtained using a simple linear least squares optimization. A second advantage over other models is the introduction of delayed oscillatory and diffusive parts of the impedance operator. This delay has a physical meaning, related to the time it takes for the wave to travel within the liner cavity and back. Using delayed first-order ordinary differential equations, the OD-TDIBC approach generalizes the EHR model. Extensions of the OD-TDIBC to a non-linear impedance model were detailed in Ref. [28, Sec. 4], demonstrating that the use of the scattering operator (i.e., the reflection coefficient) was numerically more efficient than the impedance operator in the non-linear case, while remaining equivalent in the linear case. Alternatively, an ADE method developed by Troian et al. [29] also proved capable of a broadband representation, with the difference from Ref. [27] that no delay was required in the rational function used to fit the impedance curve in the frequency domain.

In a recent study, Diab et al. [30] demonstrated that the poles and weights of the ADE-TDABC (where "A" stands for admittance, i.e., the inverse of impedance) were continuously varying with respect to the particle velocity. This property resulted in a seamless incorporation of the non-linear contribution of SDoF liners in the time domain.

CAA codes that rely on the TDIBC concept are typically high-order codes featuring low numerical dissipation to accurately solve small-amplitude waves propagating over long distances. Spatially-discontinuous numerical schemes are particularly well-suited for such problems, as the order of their approximation can be locally increased through compact stencils where contiguous elements communicate through boundary fluxes. Examples of such schemes are the Spectral Difference (SD [31]) and the Discontinuous Galerkin (DG [32, 33]) methods. Effective boundary condition management is critical to these codes and can be efficiently handled using the Navier-Stokes Characteristic Boundary Conditions (NSCBC [34]) formalism, of which TDIBCs are a subset. The main objective of a TDIBC in such schemes is to provide the characteristic entering the domain, which is a convolution of the wave exiting the domain and the reflection operator. The OD-TDIBC of Monteghetti et al. has been integrated within a DG code with the linearized Euler equations in Refs. [27, 28], in an SD code with the full Navier-Stokes equations in Ref. [35], as well as a high-order version of a second-order finite volume code with the Navier-Stokes equations in Refs. ([36], [37, II.3-II.4]).

Whatever the approach, their DoFs (i.e. the poles, weights and delays for the OD representation) must be fitted to impedance data, sometimes obtained experimentally. The quality of the approach is directly linked to the quality of this fit, and consequently, to the characteristics of the impedance. Recent advances in the state-of-the-art of liner design rely on the parallel assembly of materials having different impedances in order to extend the frequency range of absorption (see Ref. [38] for a review of recent liner concepts). Additionally, multi-stage liners - such as the stacking of two SDoFs - can be considered, rendering a single delay inadequate to represent the wave behavior. Therefore, extending the conventional TDIBC approach to complex liners might be challenging.

The conventional TDIBC modeling approach has often relied on fitting parameters to approximate the impedance operator rather than directly computing the convolution. This could be due to computational and memory cost considerations that existed at the time of the pioneering works on TDIBCs. However, with the current availability of high-performance computing resources and fast Fourier transform (FFT) libraries, a direct computation of the convolution may no longer be a bold approach. The present study aims to show that a parameter-free method, based on inverse Fourier transforming the impulse response of the scattering operator, is a promising alternative for both linear and non-linear problems.

The present manuscript introduces a TDIBC formulation that is inherently wider band than the numerical scheme considered, has the ability to handle discontinuous waves and non-linear responses alike, and does not require additional parameter fitting. The manuscript is structured as follows. In Sec. 2 we provide a review of the modeling of aeroacoustic liners and discuss non-linear effects. In Sec. 3 we introduce the proposed TDIBC method, first by tackling the linear regime before moving on towards the non-linear one. Validation cases of the method are given in Sec. 4, and numerical applications in a 2D duct are gathered in Sec. 5. Lastly, we provide an extensive discussion of our findings in Sec. 6.

2 Aeroacoustic liner impedance modeling

This section provides an overview of aeroacoustic liners and their modeling. A more comprehensive discussion including novel liner concepts is available in Ref. [38].

2.1 Physics of the dissipation within liners

Typical acoustic treatments, such as SDoF liners, consist of a perforated plate backed by a cavity [39, 40]. The primary mechanism of dissipation in these treatments occurs through viscous and thermal effects in and around the perforations [41]. The cavity introduces a delay in the wave's travel time, which can lead to constructive interference (phase match) between incoming and reflected waves at certain wavelengths. At these resonant frequencies, the acoustic particle velocity in the perforations increases, leading to additional viscous dissipation.

In the frequency domain, locally-reacting acoustic liners are defined by their *normalized* surface impedance, denoted by the complex frequency-dependent quantity $\tilde{\mathcal{Z}}$. This impedance represents the transfer function between the acoustic pressure $\tilde{p}$ and the normal velocity $\tilde{\boldsymbol{u}} \cdot \boldsymbol{n}$ at the liner surface, where $\boldsymbol{n}$ is the unit normal vector pointing into the liner surface by convention:

$$\tilde{\mathcal{Z}} = \frac{1}{z_0} \frac{\tilde{p}}{\tilde{\boldsymbol{u}} \cdot \boldsymbol{n}}, \tag{1}$$

with z_0 being the characteristic impedance of air. As was shown in different numerical studies [42, Sec .1.3.2],[28], the impedance is not particularly convenient in numerical codes due to its unbounded nature. It is more practical to work directly with the scattering operator, i.e., the reflection coefficient $\tilde{\mathcal{R}}$. This coefficient describes the ratio of the reflected wave to the incident wave and is defined as:

$$\tilde{\mathcal{R}} = \frac{\tilde{\mathcal{Z}} - 1}{\tilde{\mathcal{Z}} + 1}. \tag{2}$$

It has been established in Ref. [41] that perforated plates can be approximated as porous foams with particular properties. As cavities are commonly composed of honeycomb layers, representing each element of a liner by a porous material greatly simplifies its modeling. By using the transfer matrix approach [43, Chap. 11], one can relate the acoustic pressure and velocity fields on either side of a material layer, such as a plate or a cavity. By multiplying the matrices of each layer sequentially, the global surface impedance of the assembly can be determined. One significant advantage of this method is its ability to handle more complex situations, such as stacking multiple SDoF liners or introducing porous media like foams within cavities.

The main objective of this paper is not to provide a detailed model for the impedance of a liner. Instead, the TDIBC developed in this work is model-agnostic and requires no fitting of parameters, so the reader has the liberty to choose among the variety of impedance models available in the literature [38]. For pedagogical purposes, the considered normalized impedance for a SDoF liner is that of Atalla and Sgard [41, Eq. 8], where the wave number k_c of the cavity is that of Bruneau [44, § 3.7]:

$$\tilde{\mathcal{Z}}_{\mathrm{SDOF}}(\omega) = \frac{R_s}{c_f \phi_p}\left(\frac{2L_p}{r_p} + 4\frac{\epsilon_e}{r_p}\right)(1+\mathrm{j}) + \frac{1}{c_f\phi_p}\left(2\epsilon_e + L_p\right)\mathrm{j}\omega + \frac{1}{\phi_c}\coth\left(\mathrm{j}\tilde{k}_c L_c\right), \tag{3}$$

$$\epsilon_e = 0.85 r_p\left(1 - 1.14\sqrt{\phi_p}\right), \qquad \text{Correction length} \tag{4}$$

$$R_s = \frac{1}{2}\sqrt{2\eta\omega\rho_f}, \qquad \text{Surface resistance} \tag{5}$$

$$\mathrm{j}\tilde{k}_c = \frac{\mathrm{j}\omega}{c_f}\left[\frac{1 + (\gamma - 1)\,\Phi\left(k_\kappa r_c\right)}{1 - \Phi\left(k_\nu r_c\right)}\right]^{1/2}, \qquad \text{Cavity wavenumber} \tag{6}$$

$$\Phi(s) \coloneqq \frac{2}{s}\frac{I_1}{I_2}(s). \tag{7}$$

In the previous equations, L_p is the thickness of the perforated face sheet, ϕ_p its porosity, r_p the radius of its perforations. Similarly, L_c, ϕ_c and r_c define the honeycomb cavity properties. The ambient air is defined by its speed of sound c_f, density ρ_f, the ratio of specific heat constants γ, the dynamic viscosity η, the cinematic viscosity ν and the thermal conductivity κ. The modified Bessel functions of the first kind of order n are written I_n, and $k_\nu = \sqrt{\mathrm{j}\omega/\nu}$, $k_\kappa = \sqrt{\mathrm{j}\omega/\kappa}$.

2.2 Non-linear modeling

Typical jet engines may exhibit SPLs in excess of 160 dB inside the engine nacelle, where liners are typically installed. While non-linear effects of the ambient gas are significant for SPLs exceeding 160 dB, the non-linear aspect of perforated plates can already manifest itself at a SPL of 130 dB or lower. At high SPLs, the flow of air near the perforations can trigger a vortex-shedding mechanism, which converts the irrotational acoustic wave into rotational flow features [11]. The resulting vortices are eventually broken down and dissipated by viscosity. In experiments, the real part of the impedance was shown to increase when the SPL was raised. At resonance, while the imaginary part was slightly reduced (see e.g. Ref. [45] for a discussion on the non-dimensional coefficients that can be used to model a non-linear "thin" orifice impedance). Typical models for liners tend to represent this non-linearity as

$$\tilde{\mathcal{Z}}_{\mathrm{NL}} = \tilde{\mathcal{Z}} + \mathscr{G}_{\mathrm{NL}}(v), \tag{8}$$

where v is the acoustic particle velocity *just outside* the perforation, and $\mathscr{G}_{\mathrm{NL}}$ is a non-linear function of v (see e.g. Refs [46, 47]). The velocity within the perforation is a function of both the incoming wave and the one that has traveled within the cavity and back, adding a layer of complexity in the time-domain modeling. As shown by Billard et al. [48], even the simple Guess model [47] can be predictive, provided that the velocity within the perforations is accurately estimated. Since the velocity depends on the reflection coefficient, which itself depends on the velocity, an iterative loop is required, with an increasing number of iterations needed as the SPL rises.

An example of impedance, considered for pedagogical purposes, is that of a SDoF used in the literature for benchmarks, the GE03 NASA sample [49]. Table 1 presents the properties of the GE03 NASA sample, and Fig. 1 shows its theoretical impedance for different *incident* SPLs. The calculations are directly performed in the frequency domain at each frequency, and an iterative loop is carried out to converge on the value of v [48].

3 Direct convolution approach in the time domain

This section introduces the concept of the impulse-response TDIBC, abbreviated as IR–TDIBC. The IR-TDIBC is a technique that relies on a direct convolution to implement the TDIBC using the impulse response of the reflection coefficient. The latter is obtained by iFT. The linear and non-linear scenarios of this approach are described in Sec. 3.1 and Sec. 3.2, respectively.

Table 1: SDoF sample properties, from Ref. [49]

	GE01	GE03
Facesheet porosity (%)	8.7	15
Facesheet thickness (mm)	0.635	
Perforation diameter (mm)	1	
Sample thickness (mm)	38.1	

3.1 Linear convolution

A frequency-domain transfer function $\tilde{\mathcal{R}}$ and its corresponding time-domain equivalent $\mathcal{R}\left(t\right)$ are considered, which are related by the iFT as

$$\mathcal{R}\left(t\right) = \frac{1}{2\pi}\int_{0}^{+\infty} \tilde{\mathcal{R}}\left(\mathrm{j}\omega\right)\mathrm{e}^{\mathrm{j}\omega t}\mathrm{d}\omega. \tag{9}$$

Let $x\left(t\right)$ be an input signal and $y\left(t\right)$ the output of a linear time invariant system defined by the IR operator $\mathcal{R}\left(t\right)$. In the linear case,

$$\begin{aligned} y\left(t\right) &= x\left(t\right) * \mathcal{R}\left(t\right), \\ y\left(t\right) &= \int_{0}^{+\infty} x\left(\tau\right)\mathcal{R}\left(t-\tau\right)\mathrm{d}\tau. \end{aligned} \tag{10}$$

The input $x\left(t\right)$ can be considered as a series of appropriately scaled Dirac pulses, so Eq. 10 can be approximated at time t_N as

$$y\left(t_N\right) = \sum_{n\in[0,N]} x\left(t_n\right)\mathcal{R}\left(t_N - t_n\right), \tag{11}$$

where $t_n = n \times \mathrm{dt}$, with $\mathrm{dt} > 0$ being the simulation time step. If the impulse response $\mathcal{R}\left(t\right)$ is known, one can store it in an array of size N_R

$$\boldsymbol{R} = \begin{bmatrix} \mathcal{R}\left(t=0\right) \\ \vdots \\ \mathcal{R}\left(t=\left(N_R-1\right)\times\mathrm{dt}\right) \end{bmatrix}, \tag{12}$$

with the first element of the array being the *instantaneous response* of the operator, and the remaining elements representing the *future response*. Such an impulse response is partly shown for material GE03 in Fig. 2, where successive reflections are displayed. These reflections correspond to the back and forth travel of waves in the liner cavity. Reflections also occur at the junction between the perforated plate and the cavity, and are too concentrated in time to be separated on the signal. The total size of $\boldsymbol{R}$ depends on dt and can be quite large (in the remainder of this paper, $N_R \approx 3\cdot 10^4$). For materials such as liners, later reflections contain less energy as the signal gets dissipated. One way to alleviate the memory burden introduced by the impulse response is thus to *cut* the signal once the energy has sufficiently decreased. This strategy comes at a price in terms of precision, as it removes future reflections from the signal, but might suffice for engineering purposes since these echos usually amount to a lesser proportion of the total energy. Using an energy criterion, one can then select the lowest integer $N_\epsilon < N_R$ that respects

$$\sum_{n=1}^{N_\epsilon}\mathcal{R}^2\left(t_n\right) \geq \epsilon\sum_{n=1}^{N_R}\mathcal{R}^2\left(t_n\right) \tag{13}$$

meaning that at least ϵ of the energy contained in the IR is conserved (typically $\epsilon = 0.99$). Lowering ϵ also lowers N_ϵ. In practice, if the frequency response of the reflection coefficient is known, one can obtain $\boldsymbol{R}$ with an iFT. We fix $\epsilon = 1$ in the remainder of this paper, and the entire IR obtained by iFT is used.

Let us define the array

$$\boldsymbol{R}_n = \begin{bmatrix} \mathcal{R}\left(t=n\times\mathrm{dt}\right) \\ \vdots \\ \mathcal{R}\left(t=\left(N_R-1\right)\times\mathrm{dt}\right) \\ \left.\begin{matrix} 0 \\ \vdots \\ 0 \end{matrix}\right\} n \end{bmatrix}, \tag{14}$$

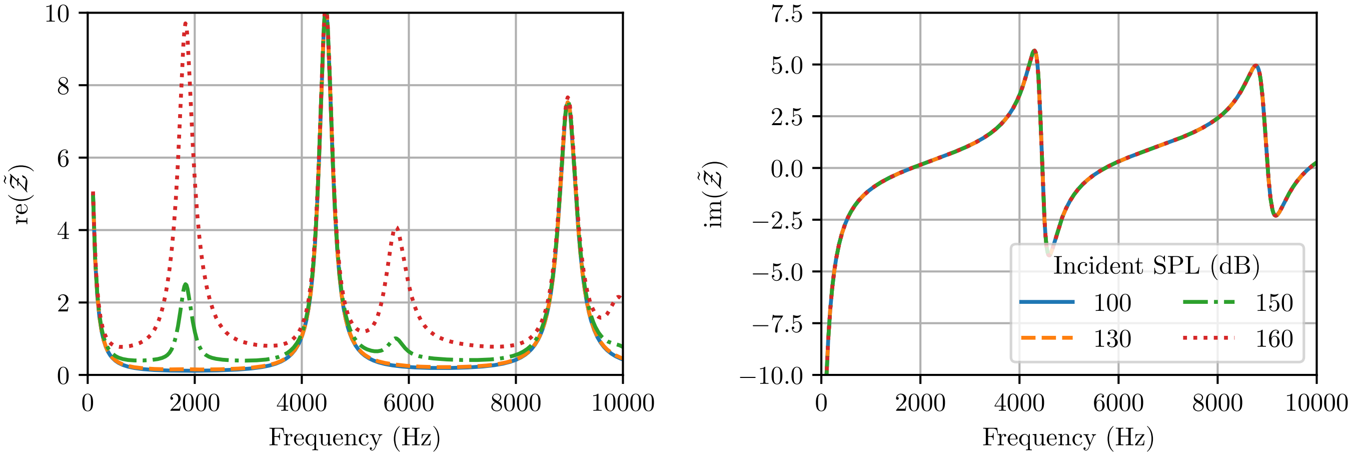

(a) Real part of the impedance

(b) Imaginary part of the impedance

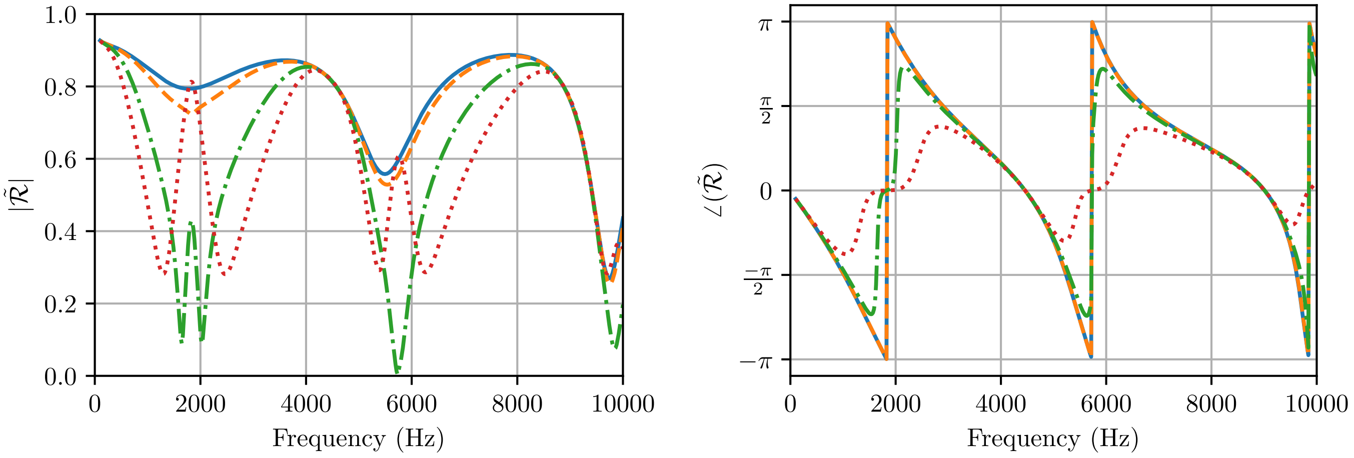

(c) Absolute value of the reflection coefficient

(d) Phase of the reflection coefficient

Figure 1: Acoustic characteristics of the GE03 sample

also of size N_R, which represents the impulse response starting at a later time $n \times \mathrm{dt}$, completed with zeros to account for the lack of information on the impulse response after the time $(N_R - 1) \times \mathrm{dt}$. We note that $\boldsymbol{R}_0 = \boldsymbol{R}$. For brevity, an index-shifting *linear operator* $\boldsymbol{\Psi} = \delta_{i,i+1}$ of size $N_R \times N_R$ is defined, with δ being the Kronecker delta. The $\boldsymbol{\Psi}$ operator transforms an array as

$$\boldsymbol{\Psi} \begin{bmatrix} a_0 \\ \vdots \\ a_{N_R-1} \end{bmatrix}_{N_R} = \begin{bmatrix} a_1 \\ \vdots \\ a_{N_R-1} \\ 0 \end{bmatrix}_{N_R} , \tag{15}$$

which resembles an array-rolling operation. One obtains the following relationship

$$\boldsymbol{R}_n = \boldsymbol{\Psi}\left(\boldsymbol{R}_{n-1}\right) = \boldsymbol{\Psi}^n\left(\boldsymbol{R}\right). \tag{16}$$

We can now define an array $\boldsymbol{y}_N$ of size N_R that contains the future response of the TDIBC once it has *seen* a discrete

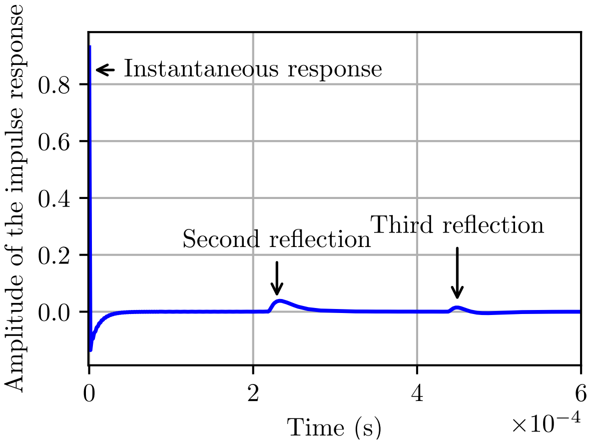

Figure 2: Impulse response $\mathcal{R}\left(t\right)$ for the GE03 sample

set of successive inputs up to a time t_N as

$$\boldsymbol{y}_N = \sum_{n\in[0,N]} x\left(t_n\right)\boldsymbol{R}_{N-n} = x\left(t_0\right)\begin{bmatrix}\mathcal{R}\left(t=N\times\mathrm{dt}\right)\\ \vdots\\ \mathcal{R}\left(t=\left(N_R-1\right)\times\mathrm{dt}\right)\\ 0\\ \vdots\\ 0\end{bmatrix}_{N_R} + \ldots + x\left(t_N\right)\begin{bmatrix}\mathcal{R}\left(t=0\right)\\ \vdots\\ \vdots\\ \vdots\\ \vdots\\ \mathcal{R}\left(t=\left(N_R-1\right)\times\mathrm{dt}\right)\end{bmatrix}_{N_R}. \tag{17}$$

A salient feature of this representation is that it can be used to build $\boldsymbol{y}_N$ iteratively, with the linearity property of $\boldsymbol{\Psi}$, as

$$\begin{aligned}\boldsymbol{y}_N &= x\left(t_N\right)\boldsymbol{R} + \sum_{n\in[1,N-1]} x\left(t_n\right)\boldsymbol{R}_{N-n}\\ &= x\left(t_N\right)\boldsymbol{R} + \sum_{n\in[1,N-1]} x\left(t_n\right)\boldsymbol{R}_{N-1+1-n}\\ &= x\left(t_N\right)\boldsymbol{R} + \sum_{n\in[1,N-1]} x\left(t_n\right)\boldsymbol{\Psi}\left(\boldsymbol{R}_{N-1-n}\right)\\ &= x\left(t_N\right)\boldsymbol{R} + \boldsymbol{\Psi}\left(\boldsymbol{y}_{N-1}\right),\end{aligned} \tag{18}$$

leading to an efficient numerical handling. One can update $\boldsymbol{y}_{N-1}$ by shifting the position of its elements by one, and by adding the time-local contribution of amplitude $x\left(t_N\right)$. Lastly, the output at the current time step $y\left(t_N\right)$ becomes

$$y\left(t_N\right) = \boldsymbol{y}_N\left[1\right],\ \forall N > 0, \tag{19}$$

where the bracket denotes the access to an array element (here the first one) which encompasses the instantaneous response due to the Dirac pulse at time t_N, as well as the integrated contribution of past time steps. This procedure recalls in essence the Duhamel principle of superposition, by means of which one integrates a solution in time by considering elementary constituents (see Ref. [50] for applications in aerodynamics).

In the present study, the impulse response $\boldsymbol{R}$ is central to the method, hence the name IR–TDIBC in what follows.

3.2 Non-linear convolution

The reflection operator exhibits non-linearity due to the contribution of the acoustic particle velocity v_{pf} within the liner perforation. This velocity is a direct function of the normal particle velocity v immediately above the perforated plate. Then, conservation of mass yields

$$v_{\mathrm{pf}} = \frac{1}{\phi}v. \tag{20}$$

We hypothesize that the non-linear problem can be rewritten as a dynamic convolution, also called impulse response switching, which can be expressed in discrete-time

$$y\left(t_N\right)=\sum_{n\in[1,N]} x\left(t_n\right)\mathcal{R}\left(t_N-t_n,\, x\left(t_N-t_n\right),\, y\left(t_N-t_n\right)\right). \tag{21}$$

This technique, already in use within the electro-acoustic community to simulate non-linear devices [51, 52], involves re-evaluating the impulse response for each amplitude of the parameter driving the nonlinearity. It has to be noted that the non-linear behavior of liners has a memory effect, since the wave that has traveled back and forth within the cavity does contributes to setting the particle velocity within the perforation. However, by using Eq. 20, it is possible to determine the contribution of the outgoing wave at the current time-step, allowing for a memory-less dynamic convolution. The primary advantages of this approach over using Volterra series to describe the nonlinearity are chiefly the generality of representation of the non-linear term, the simplicity of integration of the impulse response switching method, and the lack of need for a kernel identification. A physical limitation of the approach, common to all TDIBC methods, is that once the wave has entered the liner, its future is fixed. In experiments, when the wave comes back, it can in practice be influenced again by the non-linear behavior at the perforation on its way out. This feature cannot be predicted by the current method.

The iterative procedure on $\boldsymbol{y}_N$ is now given by

$$\boldsymbol{y}_N=x\left(t_N\right)\boldsymbol{R}\left(x\left(t_N\right),\, v\left(t_N\right)\right)+\boldsymbol{\Psi}\left(\boldsymbol{y}_{N-1}\right). \tag{22}$$

In contrast to the linear scenario described previously, the impulse response $\boldsymbol{R}$ now constitutes a non-linear function of the input and output. This is attributed to its dependence on v, a quantity that can be accessed during runtime in numerical solvers. Note that for broadband signals, it may be more relevant to consider the root mean square velocity integrated across the entire frequency spectrum, as done by Diab et al. [30].

The procedure to use the non-linear convolution approach in a code is as follows:

1. Evaluate numerically the normal acoustic particle velocity v at the TDIBC
2. Using a chosen model for the nonlinear behaviour, evaluate the non-linear contribution to the impedance, $\mathscr{G}_{\text{NL}}\left(v\right)$. The detailed description of one such model is delayed to Sec. 4.3.
3. Following Eq. 8, evaluate the total impedance $\tilde{\mathcal{Z}}_{\text{NL}}$ in the frequency-domain, which is the sum of the linear contribution $\tilde{\mathcal{Z}}$ and the non-linear contribution $\mathscr{G}_{\text{NL}}\left(v\right)$.
4. Evaluate the corresponding reflection coefficient $\tilde{\mathcal{R}}$ using Eq. 2.
5. Calculate the corresponding IR, $\boldsymbol{R}$, and use it to update $\boldsymbol{y}_N$ in Eq. 22

4 Validations

We start by validating the IR–TDIBC technique on a straightforward input-output solver, presented as supplementary data in the form of a python script. The linear solver is first demonstrated on the impedance of the GE03 sample in Sec. 4.1, and the non-linear case is treated in Sec. 4.3. The considered configuration is quite representative of the impedance tube measurement set-up, depicted schematically in Fig. 3. For the purpose of this validation, the propagation aspect of the incident and reflected waves is deemed unnecessary. Only signals originating locally at the TDIBC surface, i.e., at the sensor position in Fig. 3, are taken into account.

4.1 Linear case

Two incident waves are considered in the linear case. The first one is a continuous pulse, while the second is a discontinuous signal. Their evolution in time at the sensor location ($x=L$) is shown in Figs. 4–5. Knowing the full time-domain incident signal $F_{\text{in}}\left(t\right)$ and the frequency-domain scattering operator $\tilde{\mathcal{R}}$, the exact expression of the reflected wave at $x=L$ is

$$F_{\text{out}}\left(t\right)=\text{iFT}\left(\tilde{F}_{\text{in}}\left(\omega\right)\cdot\tilde{\mathcal{R}}\left(\omega\right)\right), \tag{23}$$

where $\tilde{F}_{\text{in}}\left(\omega\right)$ is the FT of $F_{\text{in}}\left(t\right)$. $F_{\text{out}}\left(t\right)$ is considered as the reference solution. It is here evaluated by means of the FFT algorithm. This direct approach to calculating $F_{\text{out}}\left(t\right)$ cannot be applied in numerical codes for wave propagation, since one does not know the entirety of the incident wave signal in advance. Using the IR–TDIBC approach described in Sec. 3.1, $F_{\text{out}}\left(t\right)$ can now be calculated iteratively. Prior to this calculation, the first step is to evaluate $\boldsymbol{R}$, which

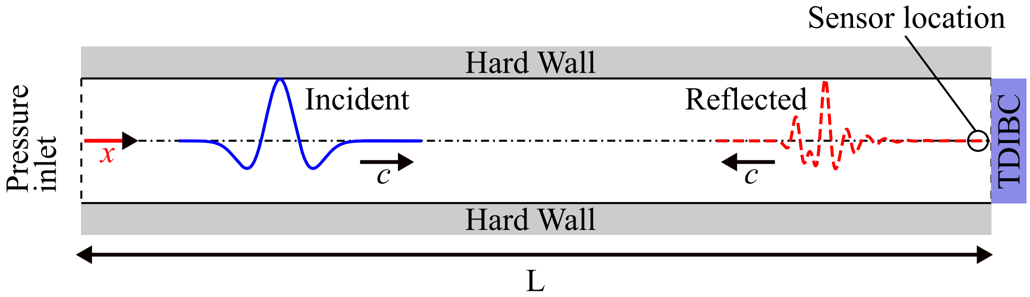

Figure 3: Setup of the impedance tube test case. A right-running pressure wave enters the domain at $x = 0$ and impacts the TDIBC at $x = L$, where it is reflected back towards the inlet.

is done via an iFT applied to $\tilde{\mathcal{R}}(\omega)$. The time step of the simulation is $\mathrm{dt} \approx 1.5 \cdot 10^{-6}$ s, in line with the envisioned time steps encountered in CAA simulations. The total simulation time is $5 \cdot 10^{-2}$ s. The high frequency limit related to Shannon's theorem is thus much higher (330 kHz) than the typical frequency content of interest in aero-acoustics (20 kHz). The match between the reflected waves obtained with the IR–TDIBC algorithm and the reference ones are displayed in Fig. 4b–5b, showing a perfect agreement. Handling discontinuous signals with the IR-TDIBC approach is done in a natural way, since at its root, the method is based on a Dirac pulse input, see Fig. 5b. At the onset of the discontinuous signal, the reference solution displays an oscillation, shown in the inserted zoom of Fig. 5b. The oscillation is attributed to a Gibbs phenomenon, a standard feature of the FFT for discontinuous signals. The signal obtained from the IR-TDIBC is exempt from spurious oscillations near the discontinuity, because the FFT used to calculate the IR is applied on a continuous quantity, the reflection coefficient.

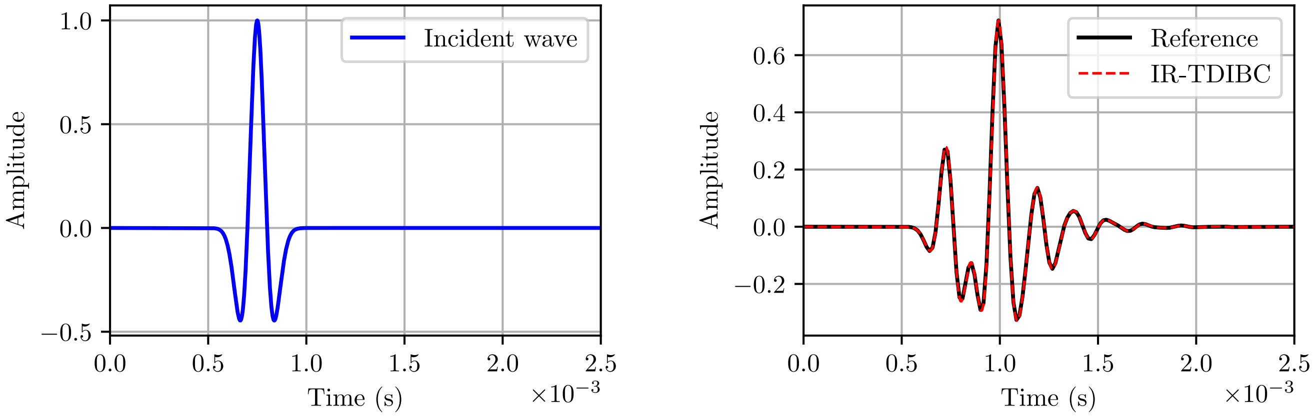

(a) Incident wave

(b) Reflected waves

Figure 4: Numerical test of the linear IR–TDIBC. Incident and reflected waves for the GE03 sample with a continuous wave. Comparison with the reference result, obtained via iFT on the entire signal.

Using the reflected wave in the time domain (the data displayed in Fig. 4b for instance), one can re-evaluate the reflection coefficient in the frequency domain, or alternatively the surface impedance that has been imposed by the IR–TDIBC. The comparison between these values and the theoretical ones obtained in Eq. 3 are displayed in Fig. 6, where the continuous input signal was used. The fit is excellent up to 25 kHz, but the IR–TDIBC solution deviates from the theory beyond this frequency. The continuous incident wave has an energy spectrum contained below 25 kHz, so there is not enough signal for the post-processing to be meaningful at higher frequencies. Increasing the frequency content of the incident signal, for instance by considering the discontinuous signal of Fig. 5a, one can recover a perfect fit up to higher frequencies too.

4.2 Extension to complex liners

A challenging class of liners to model with classical TDIBC approaches is that of multi-degree-of-freedom (MDoF) liners, which comprise a series of SDoF liners stacked on top of one another. MDoF liners pose significant difficulties,

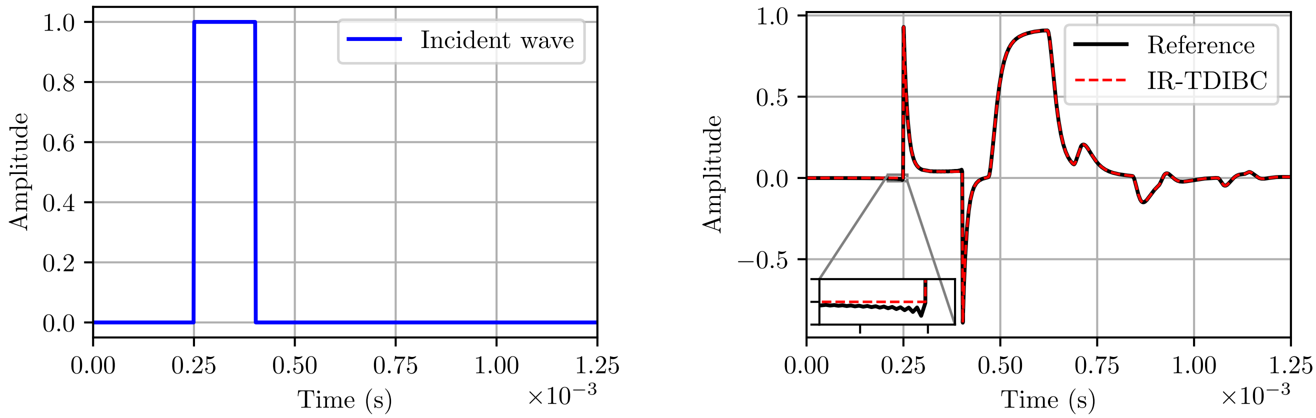

(a) Incident wave

(b) Reflected waves

Figure 5: Numerical test of the linear IR-TDIBC. Incident and reflected waves for the GE03 sample with a discontinuous wave. Comparison with the reference result, obtained via iFT on the entire signal.

owing to the presence of delayed differential equations associated with each cavity that lead to an increased number of parameters caused by the rise in the number of resonances and anti-resonances in a particular frequency band. Another relevant problem in the field of aeroacoustic liners concerns the characterization of an acoustic metasurface, which is a parallel assembly of SDoF liners. The total impedance $\tilde{\mathcal{Z}}_{\mathrm{tot}}$ of a parallel assembly of P liners, each of impedance $\tilde{\mathcal{Z}}_p$, is given by

$$\tilde{\mathcal{Z}}_{\mathrm{tot}} = \left[\sum_{p=1}^{P} \frac{1}{\tilde{\mathcal{Z}}_p}\right]^{-1}. \tag{24}$$

By combining the two concepts previously introduced, i.e. MDoF liners and the parallel assembly of P liners, one can devise intricate liners with optimized impedances, capable of absorbing sound across a broad frequency range. Such complex liners are analyzed next in order to showcase and leverage the versatility of the IR-TDIBC approach when dealing with elaborate impedance laws.

The selected liner architecture is more elaborate than the classical SDoF liner of Sec. 4.1. It is made of three different liner surfaces S_i, each of which has multiple stages. A perforated plate is considered on top of a cavity filled with a foam, and this assembly is placed on a LEONAR sample – a perforated plate with tubes extending through the cavity. A schematic of the proposed metasurface is presented in Fig. 7. In order to obtain the liner properties, we choose an optimization strategy subjected to the constraint of a fixed liner height (5 cm) responding to the incident signal $x(t)$ shown in Fig. 4a. A global optimization tool called pyMOO [53] was used to minimize the cost function $\mathcal{J}$, defined by

$$\mathcal{J} = \int_0^{t_{\max}} |x(t) * \mathcal{R}(t)|\,\mathrm{d}t = \int_0^{t_{\max}} |y(t)|\,\mathrm{d}t, \tag{25}$$

where $t_{\max}$ is the end time of the simulation, and where the parameters to be optimized appear in the calculation of the reflection coefficient, which is then used by the IR-TDIBC method to calculate the output wave $y(t)$. Some liner properties are fixed here for simplicity, including the foam intrinsic properties, such as its porosity and tortuosity. The foam is modeled in frequency domain via the Jonhson-Champoux-Allard model [54, 55] and roughly corresponds to a melamine foam, often encountered in the field of acoustics. More information on the optimization tool, called OPAL, can be found in Ref. [56]. A total of 19 parameters were optimized: the perforated plates porosities and radius of perforation, the foam thickness (taken equal in all liners), the tube length, radius and total porosity, as well as its cavity height. The reflected wave is shown in Fig. 8, showing a close to perfect agreement with the reference solution obtained via the direct convolution approach. The goodness of fit remains excellent at longer times, when most of the signal has been dissipated, as shown in the inset in Fig. 8.

Using the output of the IR-TDIBC solver, i.e., the reflected wave, the reflection coefficient and surface impedance that were effectively imposed numerically are evaluated. The comparisons between theoretical values and those obtained numerically are shown in Fig. 9. An excellent agreement is found, despite a quite complex "shape" of the reflection coefficient and impedance functions. This confirms that the IR-TDIBC solver is quite capable of handling

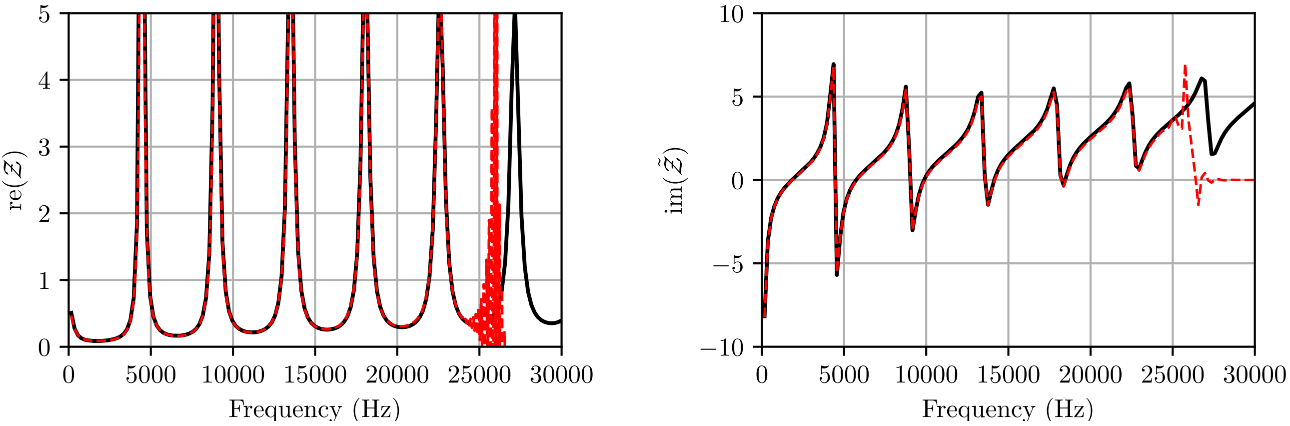

(a) Real part of the impedance

(b) Imaginary part of the impedance

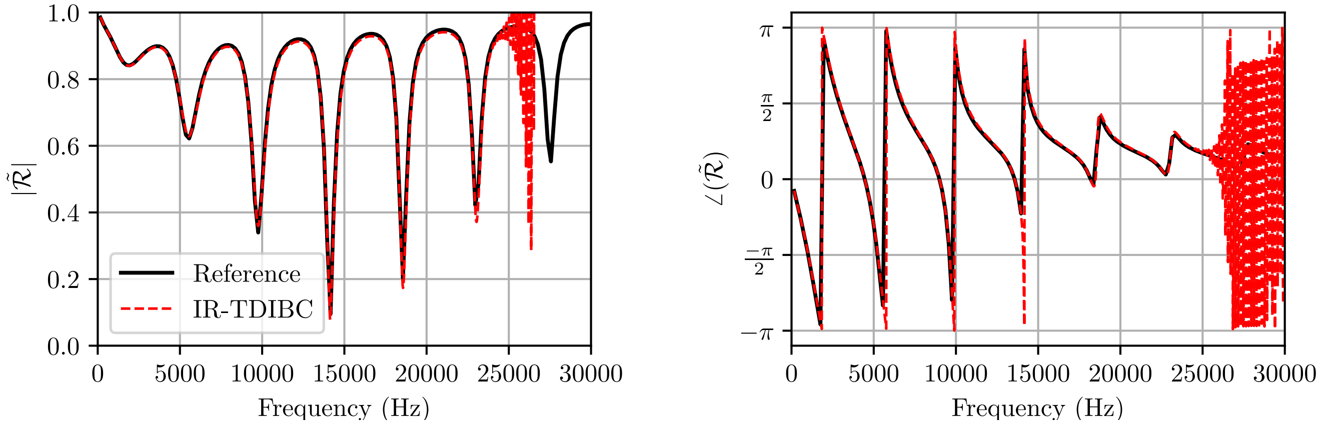

(c) Absolute value of the reflection coefficient

(d) Phase of the reflection coefficient

Figure 6: Comparisons between the exact acoustic properties and the ones obtained using the wave reflected with the IR-TDIBC approach.

most liner configurations, without any overhead in terms of calculation, nor any fitting of parameters required from the user.

4.3 Non-linear case

To validate the non-linear capabilities of the IR–TDIBC method, a dataset obtained by NASA in an impedance tube configuration is used [49], similar to that of Fig. 3. Two different acoustic liners known for their non-linear behaviors are considered at two different SPLs: 120 dB and 140 dB. The liner properties were given in Table 1, and the model described in Eq. 3 is used to evaluate their impedance. For each simulation, non-linear effects are considered, although they are expected to be small in the 120 dB case. The non-linear Guess model [47] is selected to update the impedance value as a function of the normal particle velocity at the liner surface, i.e., the non-linear contribution to the impedance in Eq. 8 becomes

$$\mathscr{G}_{\mathrm{NL}}(v) = \frac{1-\phi^2}{\phi^2}\frac{|v|}{c_f} = \alpha_{\mathrm{NL}}\,|v|\,, \tag{26}$$

where α_{NL} is the non-linear parameter. The normal particle velocity immediately outside of the perforation is v, taken along the x component in Fig. 3.

The SPL was measured in the experiment at a location very close to the upper surface of the liner, and consists in a total SPL including the contribution of both incident and reflected waves. Here, the sensor location displayed in Fig. 3 is used again as the reference location for this measurement, and thus the propagation aspect of waves in space can be ignored. An input-output relationship can be adopted, i.e. the only dimension of the problem is time.

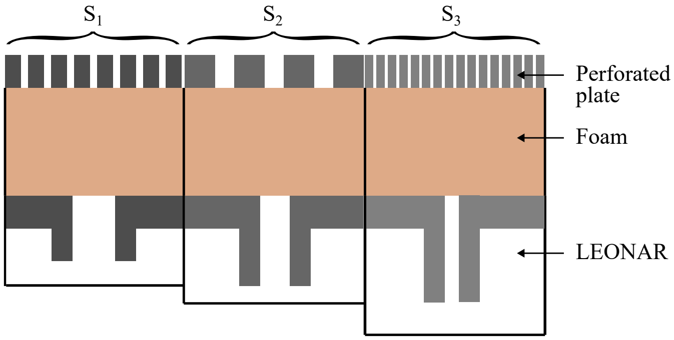

Figure 7: Schematic of the metasurface

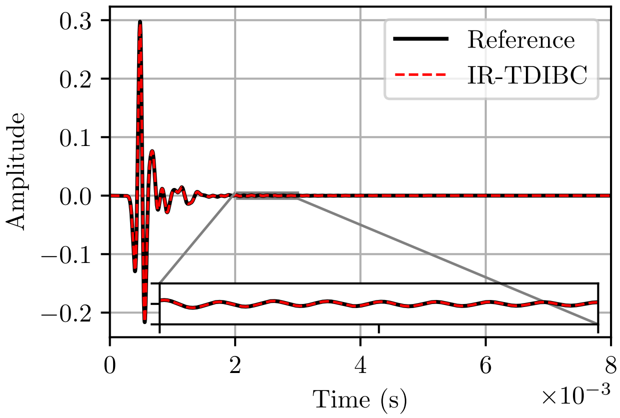

Figure 8: Reflected waves for the optimized metasurface sample. Comparison with the reference result, obtained via iFT on the entire signal.

A control system was used by NASA to modulate the loudspeaker response until a target SPL was reached at the sensor location. In a numerical solver, only the incident wave amplitude can be directly entered by the user. Due to the standing wave pattern that is present in an impedance tube, a frequency dependent SPL is observed at the liner surface. Given the non-linear behavior of the considered liners, a complex dependency can exist between the incident SPL, the total SPL and the non-linear impedance of the liner. Sine waves are considered numerically too, and the incident SPL is initialized in the simulations at the target SPL. The simulation is then run multiple times and the incident amplitude adjusted by a gradient descent approach until the target SPL is reached, within a 0.1 dB margin. In this respect, the numerical method closely matches the experimental one. The time-domain reflected signal is recorded, and then transformed back into the frequency domain, from which the reflection coefficient and the impedance are recovered at each frequency. The impedance numerically obtained for both the GE01 and GE03 liners are displayed in Figs. 10 and 11 along with the experimental data. Given the potential experimental uncertainties on the liner properties and the general variations observed between *identical* samples in round robin tests [57], the impedance realized by the IR–TDIBC approach can be considered to be a good fit to the experimental data. We note that the "peak" of the real part of the impedance, called resistance, is well captured by the model in both cases near the resonance, with a slight shift of this peak to higher frequencies in the numerical case. Accounting for a non-linear contribution to the imaginary part of the impedance could help further improve the fit, and could be achieved straightforwardly by updating Eq. 26 as needed.

5 Applications in a Spectral Difference solver

Now that the approach has been validated on both linear and non-linear cases, the IR–TDIBC approach is included in a solver capable of handling the propagation of waves in space and time, in order to represent more complex configurations. This solver, called JAGUAR, is first presented in Sec. 5.1. A grazing incidence 2D duct is then tackled numerically in Sec. 5.2, since this configuration is widely used in the impedance eduction community, where the non-linear effect on the impedance is often neglected.

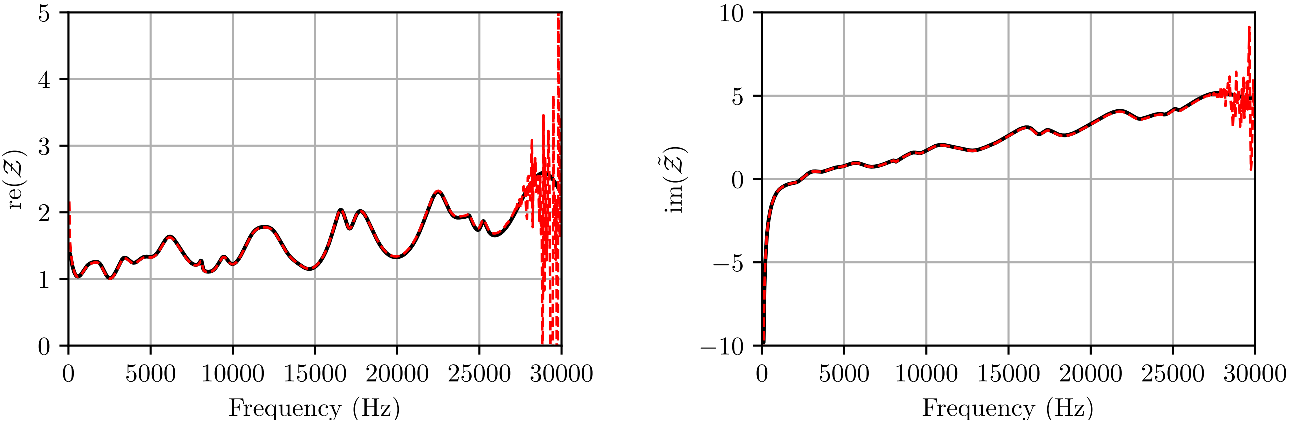

(a) Real part of the impedance (b) Imaginary part of the impedance

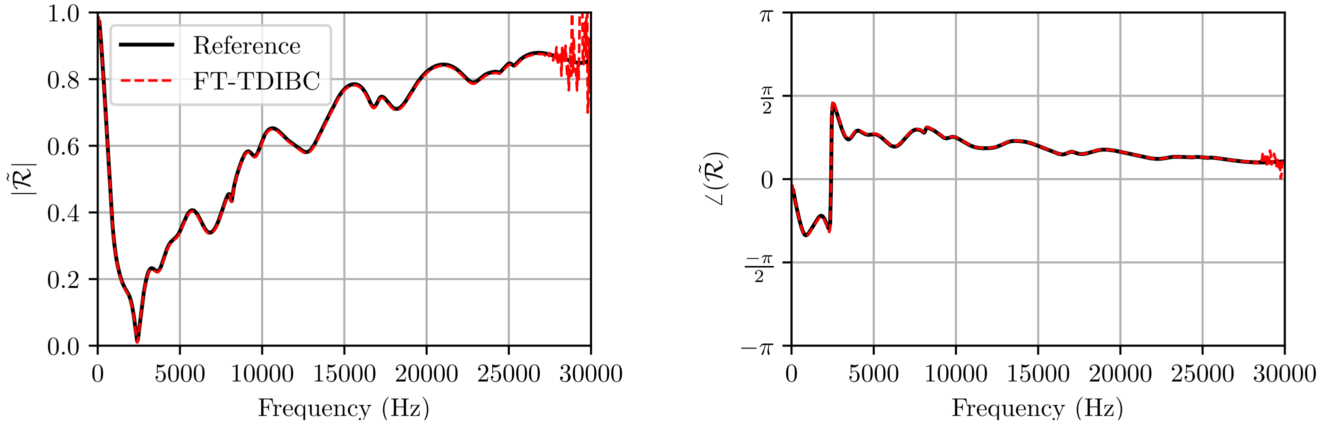

(c) Absolute value of the reflection coefficient (d) Phase of the reflection coefficient

Figure 9: Comparisons between the exact acoustic properties and the ones obtained using the wave reflected with the IR-TDIBC approach, on the optimized metasurface sample.

5.1 The JAGUAR solver for aeroacoustics

The code selected for the implementation of the IR-TDIBC is a fully non-linear Navier-Stokes solver relying on a high-order discontinuous method for the spatial discretization. Named JAGUAR [58, 59], the solver is jointly owned by CERFACS[1] and ONERA[2]. It is based on an SD scheme [31, 60–62], which handles the strong form of the governing equations. The conservative variables (hereafter, the solution) and their fluxes are approximated inside each computational cell by fitting two polynomials: one of order p for the solution and one of order $p+1$ for the fluxes. The ability to generate the additional degrees of freedom internally within the cell allows for a high-order discretization to be obtained on unstructured meshes, and hence to consider flows around complex geometries. In contrast, a high-order discretization obtained with finite differences generally requires a large computational stencil achievable only on structured grids. Throughout this study, $p = 4$, which results in a fifth-order accurate SD scheme. Furthermore, the time integration follows an optimized low-dissipation low-dispersion 6-step Runge-Kutta scheme inspired from Berland et al.[63]. Finally, all results presented in the following sections are carried out in two dimensions with the

---

[1] European Center for Advanced Training in Scientific Computation

[2] The French Aerospace Lab

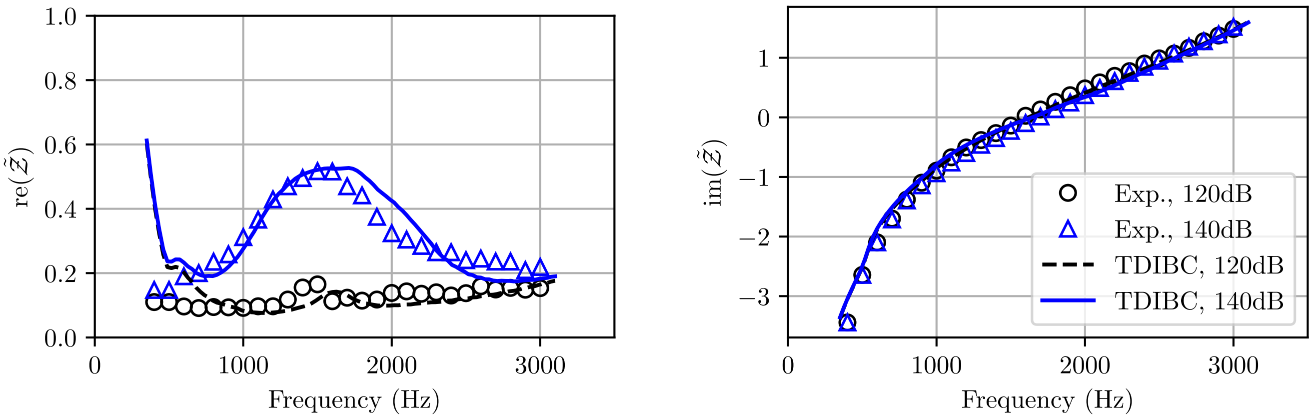

(a) Real part of the impedance

(b) Imaginary part of the impedance

Figure 10: Impedance of the GE01 sample, comparison between NASA's experiments and the present IR-TDIBC model.

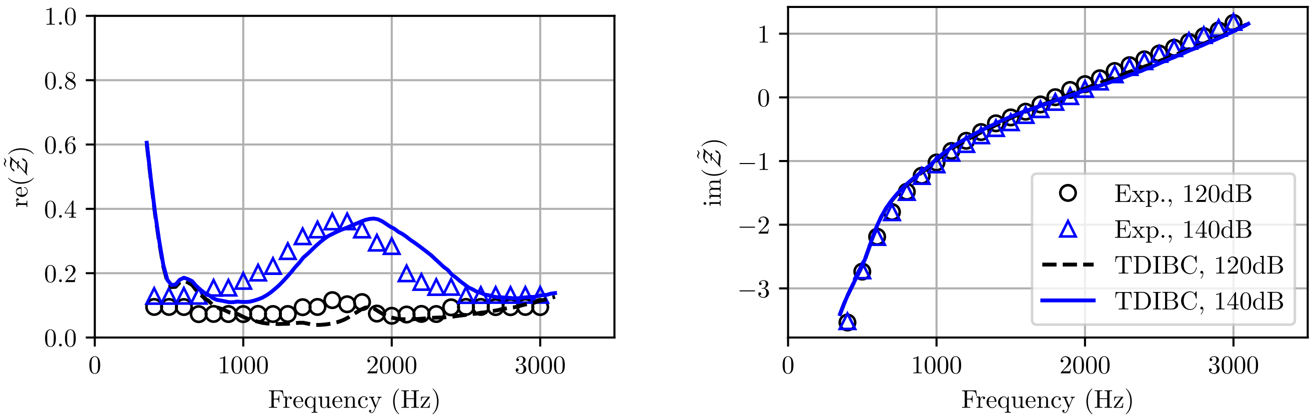

(a) Real part of the impedance

(b) Imaginary part of the impedance

Figure 11: Impedance of the GE03 sample, comparison between NASA's experiments and the present IR-TDIBC model.

Navier-Stokes equations. The governing equations in generalized coordinates (ξ,η) are given by:

$$\begin{aligned}\frac{1}{\mathcal{J}}\frac{\partial \boldsymbol{U}}{\partial t} + \frac{\partial}{\partial \xi}\left(\boldsymbol{E}_c\frac{\xi_x}{\mathcal{J}} + \boldsymbol{F}_c\frac{\xi_y}{\mathcal{J}}\right) + \frac{\partial}{\partial \xi}\left(\boldsymbol{E}_d\frac{\xi_x}{\mathcal{J}} + \boldsymbol{F}_d\frac{\xi_y}{\mathcal{J}}\right)&\\ + \frac{\partial}{\partial \eta}\left(\boldsymbol{E}_c\frac{\eta_x}{\mathcal{J}} + \boldsymbol{F}_c\frac{\eta_y}{\mathcal{J}}\right) + \frac{\partial}{\partial \eta}\left(\boldsymbol{E}_d\frac{\eta_x}{\mathcal{J}} + \boldsymbol{F}_d\frac{\eta_y}{\mathcal{J}}\right) &= 0,\end{aligned} \tag{27}$$

where $\boldsymbol{U} = [\rho, \rho u, \rho v, \rho(e + (u^2 + v^2)/2)]^\intercal$ is the solution vector. The density is labeled as ρ, the streamwise (herein x-coordinate) velocity as u, the wall-normal (herein y-coordinate) velocity as v and the specific internal energy as e.

$\mathcal{J}$ is the mesh Jacobian, and the convective and diffusive fluxes of $\boldsymbol{U}$ in physical space are $(\boldsymbol{E}_c, \boldsymbol{F}_c)$ and $(\boldsymbol{E}_d, \boldsymbol{F}_d)$, respectively. These fluxes are defined as:

$$\begin{aligned}\boldsymbol{E}_c &= (\rho u, \rho u^2 + p, \rho v u, (\rho e + p)u)^\intercal\\ \boldsymbol{F}_c &= (\rho v, \rho u v, \rho v^2 + p, (\rho e + p)v)^\intercal\\ \boldsymbol{E}_d &= (0, p + \tau_{(1,1)}, \tau_{(2,1)}, u\tau_{(1,1)} + v\tau_{(2,1)} + \lambda_T \partial_x T)^\intercal\\ \boldsymbol{F}_d &= (0, \tau_{(1,2)}, p + \tau_{(2,2)}, u\tau_{(1,2)} + v\tau_{(2,2)} + \lambda_T \partial_y T)^\intercal\end{aligned} \tag{28}$$

with viscous stress tensor $\tau_{(i,j)}$ (in kg.m^{-1}.s^{-2}) and thermal conductivity λ_T (in J.K^{-1}). The flux balance at the boundaries is modified in order to account for the NSCBCs, following the approach suggested by Kim and Joo [64]. For a validation of the NSCBCs implemented in JAGUAR in test cases of variable complexity, we refer the readers to Fiévet et al.[35], where the OD–TDIBC approach was also considered.

5.2 Grazing impedance tube configuration

The grazing incidence duct configuration, commonly used by the aeroacoustic community to test liners, is considered and described next. A two-dimensional $L \times H$ domain (in the x and y directions, respectively) is discretized with 201×12 rectangular cells of constant size, yielding 60,300 degrees of freedom at this order of approximation ($p = 4$). In our numerical discretization, $L = 812\,\text{mm}$ and $H = 50.8\,\text{mm}$. A sketch of the numerical setup, along with details on the TDIBC location, is provided in Fig. 12. The simulations for this case were run by solving the Navier-Stokes equations during a total of $1.2{\cdot}10^5$ iterations with a uniform time step of $\text{dt} = 2.5{\cdot}10^{-7}\,\text{s}$. An ambient pressure of $P_a = 101,325\,\text{Pa}$ and ambient temperature of $T_a = 295\,\text{K}$ are considered. There is no net mass flow through the domain (no flow case). Both walls are treated as hard wall isothermal BCs at ambient temperature. The fluid is air with constant specific heat ratio $\gamma = 1.4$ and sound speed $c = 344.31\,\text{m/s}$, and the viscosity varies with temperature according to Sutherland's law (reference viscosity and temperature are $\mu_{\text{ref}} = 1.715 \cdot 10^{-5}\,\text{kg}/(\text{m} \cdot \text{s})$ and $T_{\text{ref}} = 273.15\,\text{K}$, respectively).

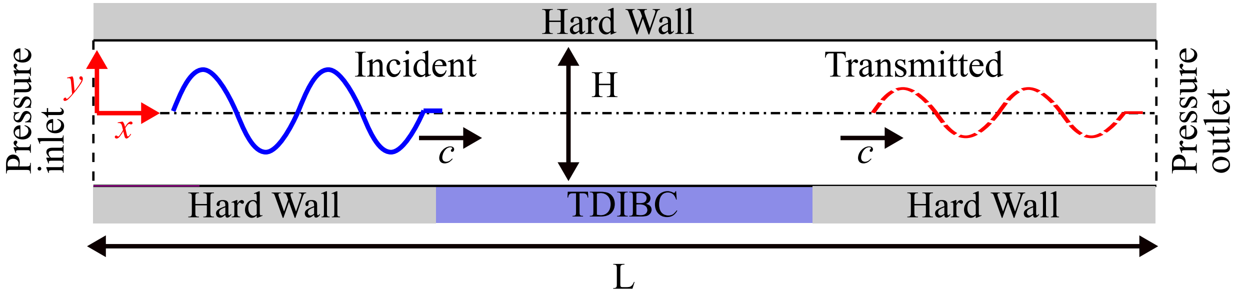

Figure 12: Setup of the grazing incidence duct test case. A right-running pressure wave first enters the domain at $x = 0$ and grazes over the TDIBC located at the lower wall, and then travels towards the exit at $x = L$.

Two theoretical liners are considered. The first one was introduced in a recent work by Diab et al. [30], where the non-linear effects were integrated by modulating the coefficients of the ADE–TDABC (the admittance was used instead of the impedance but the strategy remains similar). In addition, a second liner configuration is also considered, for which the non-linear behavior is artificially changed by increasing the value of its α_{NL}, which is given otherwise by the Guess model in Eq. 26. The properties of both samples are given in Table 2, as well as their resonance frequency f_{res}, which is the frequency at which a sine wave is generated at the inlet of the domain. The linear impedance of the materials is shown in Figure 13. The incident SPL is varied from 80 dB to 150 dB in the JAGUAR simulations.

Table 2: SDoF sample properties, from Ref. [30]

	M1	M2
Facesheet porosity (%)	1.5	20
Facesheet thickness (mm)	1	1
Perforation diameter (mm)	0.5	2
Cavity depth (mm)	10	40
α_{NL}	10.8	10.8
f_{res}(Hz)	1574.6	1731.4

In the simulations, the SPL is extracted at the upper wall opposite from the liner by calculating the FFT of the time-domain pressure signal in multiple locations, and interpolating the frequency-domain signal at the frequency of generation - i.e. the resonance frequency. The difference Δ_{SPL} in dB between the total SPL and the incident SPL is represented for the M1 liner in Fig. 14 and for M2 in Fig. 15.

The results for material M1 are qualitatively similar to those obtained by Diab et al. [30]: an increase in the SPL leads to a more resistive impedance overall, leading to less absorption in the duct. The difference between the

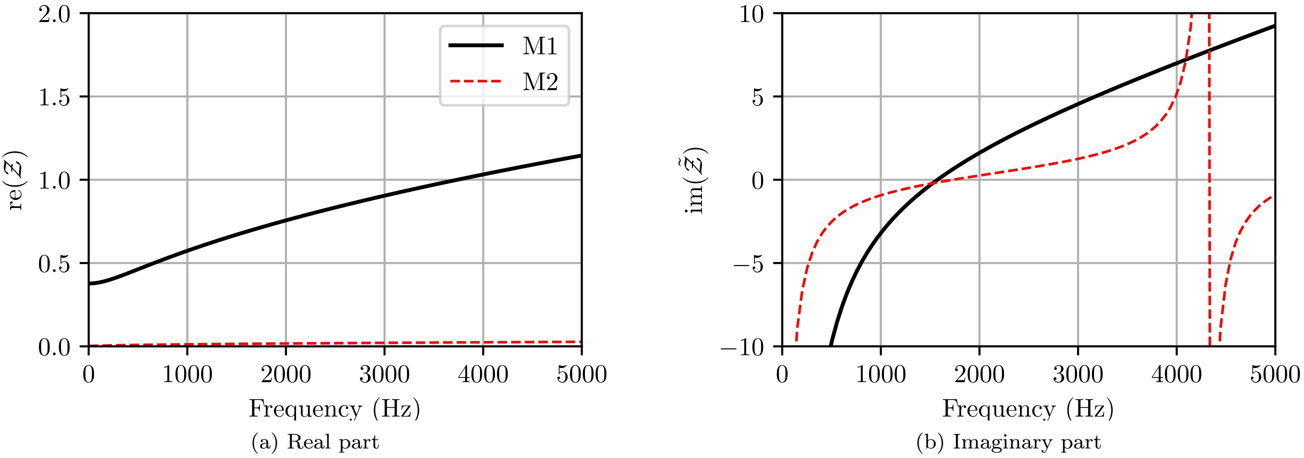

(a) Real part (b) Imaginary part

Figure 13: Surface impedance of the M1 and M2 samples

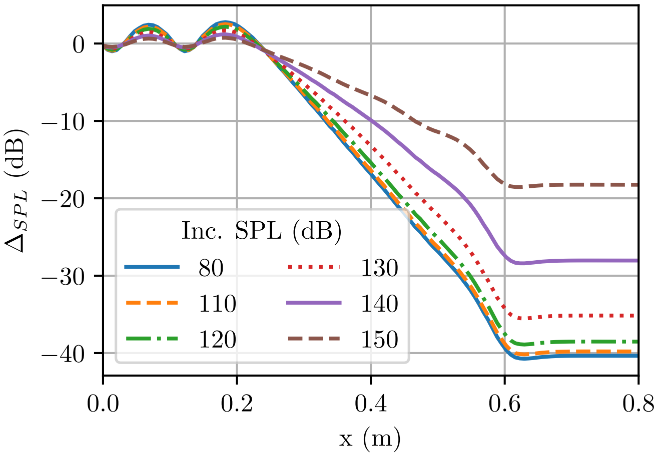

Figure 14: Spatial evolution of the SPL at the upper wall of the duct, with M1 installed.

present results and those of Ref. [30] are attributed here to a difference in the modeling of the non-linear effect. Instead of considering the non-linear contribution as a way to change the intrinsic parameters of the perforated plate (resistivity and tortuosity), the rather simplified approach of Guess was followed, directly updating the impedance by the experimental correlation of Eq. 26. The present model does not account for a change in the imaginary part of the impedance, called reactance. However, the reactance was increased in the case of Diab et al. [30] at higher SPL, resulting in less absorption in the duct since the sample was not at resonance anymore. We stress once again that the IR–TDIBC approach is model agnostic and could handle different models of non-linear behavior if needed.

The resistance at the resonance frequency is lower for material M2 than it is for M1 due to its higher porosity. The non-linear behavior, controlled by α_{NL}, is taken equal for both liners. This is not fully realistic, because a higher porosity generally incurs a lower α_{NL} [47]. There were two reasons behind the nonphysical change. The first one was to display a particular behavior, i.e. that the attenuation in the duct is improved as the SPL increases for M2, as opposed to what was observed in the case of M1. As a result of increasing the SPL and thus the resistance of the material, the impedance becomes closer to the optimal value, until an incident SPL of 140 dB is reached. After this limit, the resistance becomes too high and the attenuation decreases. The second reason behind this nonphysical change is rooted in the results obtained in Ref. [65], where an iterative method was used in the frequency domain to tackle the non-linear behavior of the impedance. One of the conclusions of that work was that for a given α_{NL}, less resistive liners would display an increased variation of the impedance across their surface.

The spatially-varying impedance is extracted at the numerical DoFs constituting the IR–TDIBC, by first considering the FFT of the pressure and normal velocity at the frequency of generation, and then calculating the ratio of both quantities. The spatially-varying impedance is given in Fig. 16 for M1 and in Fig. 17 for M2. An almost linear

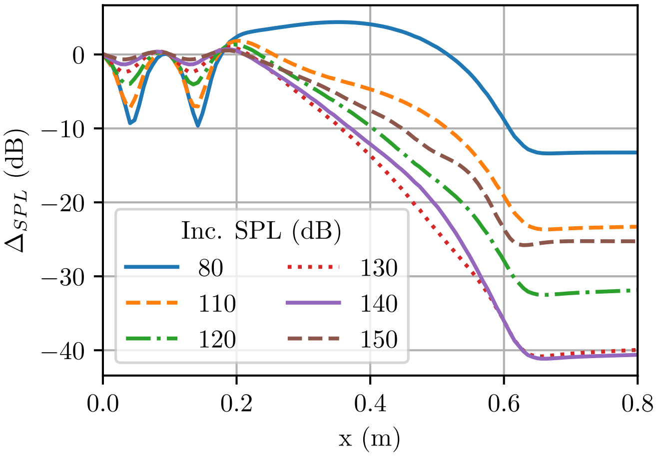

Figure 15: Spatial evolution of the SPL at the upper wall of the duct, with M2 installed.

decrease of the real part of the impedance is observed for both materials, which supports the hypothesis made by Lafont et al. [66] in an attempt to simplify the eduction process for non-linear cases.

The results obtained in Ref. [65] indicate that for a low value of the linear resistance, the real part of the spatially-varying impedance should be higher than in the case of a high value of linear resistance. This phenomenon, observed numerically, was attributed to a higher impedance discontinuity in the case of a low resistance material, which would in turn lead to a high variation of the normal particle velocity on the liner, yielding a high contribution to the resistance by nonlinear effects. As a result, a higher *nonlinear* resistance value was expected in the present work for M2, which has a low *linear* resistance value. This feature was not observed, and the difference with Ref. [65] remains unexplained. Similar results were obtained with the Euler equations in JAGUAR, meaning that the presence of viscosity in the NS equations cannot be responsible for the observed discrepancy.

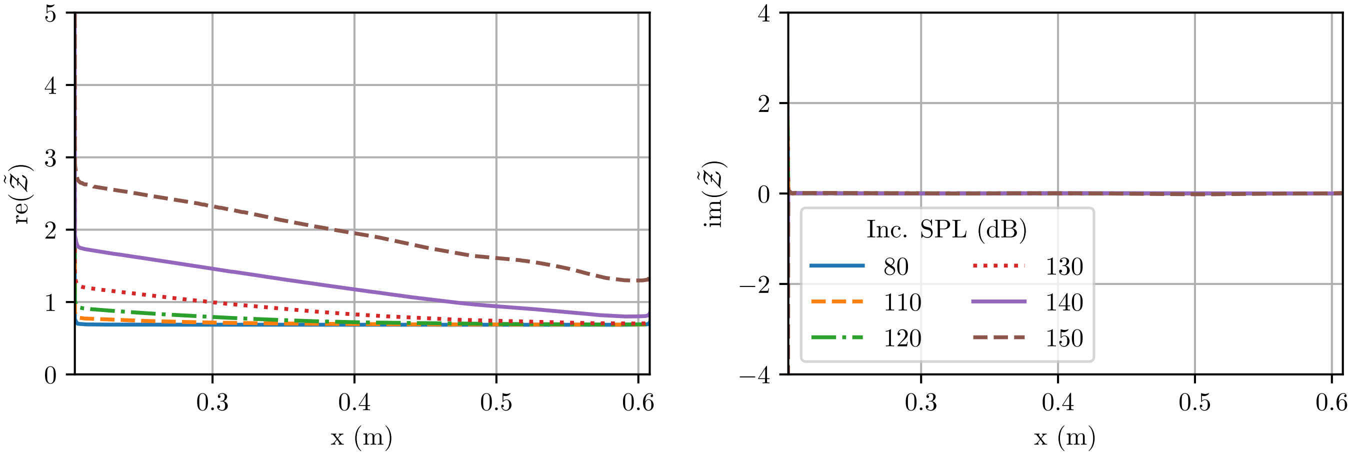

(a) Real part of the impedance

(b) Imaginary part of the impedance

Figure 16: Spatially varying impedance of M1 along the lined section

6 Discussions

This section gathers observations related to the IR–TDIBC as well as its practical implementation.

6.1 The broadband aspect

For a given simulation with a time step dt fixed in advance, the reflection coefficient is well approximated from 0 Hz up to a cut-off frequency of dt^{-1}. Simulations are naturally performed at a dt sufficiently small to extract relevant

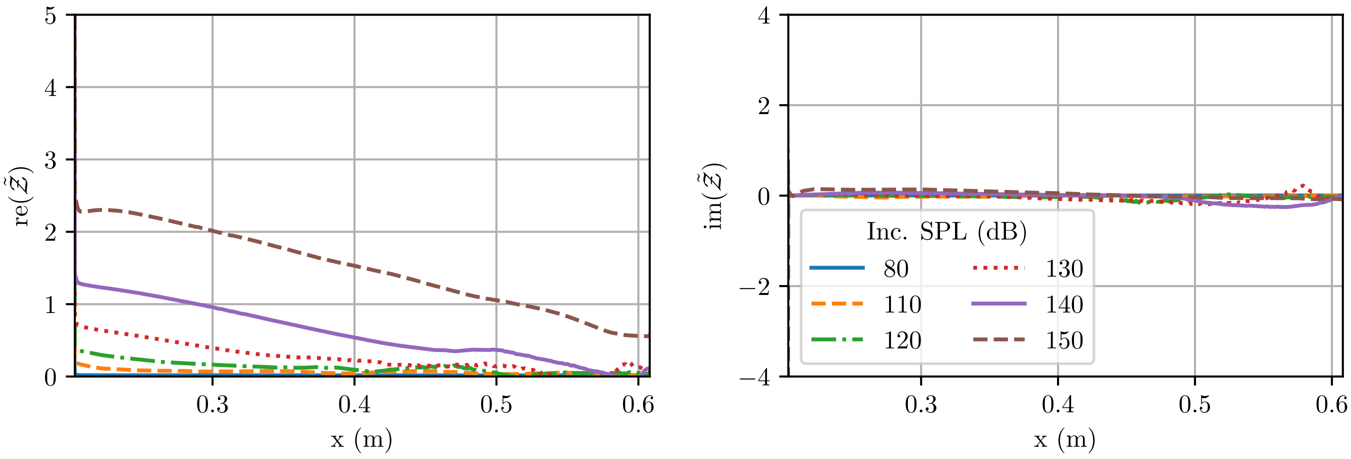

(a) Real part of the impedance

(b) Imaginary part of the impedance

Figure 17: Spatially varying impedance of M2 along the lined section

data from a signal of interest. The maximum frequency of such a signal thus needs to be lower than $0.5 \times \mathrm{dt}^{-1}$ for the sampling to respect Shannon's theorem [67].

We note in passing that we verified a power law decrease in the error for increasingly smaller time step dt, with the decay exponent imposed by the order of the time integration scheme. This check confirmed that the array-rolling procedure detailed in 3.1 preserves the order of the time integration scheme. For that validation, a fourth order Runge-Kutta was chosen in the NS solver JAGUAR, applying it to a 1D impedance tube problem with a purely reflective wall on one end. The choice of a purely reflective wall was deliberate, as that is a case where the impulse response $\boldsymbol{R}$ does not need to be recomputed by iFT for every dt selected during the error convergence study. Indeed, it remains a vector with a single one followed by zeroes, regardless of the dt employed: $\boldsymbol{R}$=[1,0,0] with $N_R = 3$. It is important to note that in more general problems, allowing the dt to shape the impulse response $\boldsymbol{R}$ will have an impact on the numerical representation of the physics in ways that go beyond those strictly related to the order of the numerical scheme, as it modifies the frequency resolution of the wave reflection process and hence the physical behavior of the IR-TDIBC. It follows that an error convergence study with a dt-dependent impulse response $\boldsymbol{R}$ would provide a result that stems from two different mechanisms: one related to the time step truncation error, and one related to the sampling resolution of the frequency-dependent IR-TDIBC.

Going back to the properties of the IR–TDIBC, we emphasize that it is *intrinsically* broadband, i.e., it can handle every signal of interest without further tuning of any parameter. By design, the method naturally handles Dirac impulses and is thus well adapted to treat discontinuous signals, without any previous knowledge input by the user. A potential drawback of the method is that it requires one to know the impedance of a sample from 0 Hz up to a frequency of dt^{-1}. While this is not a problem theoretically with current models from the literature, such as the one in Eq. 3, more complex materials whose impedance can only be obtained experimentally might prove challenging.

Extending the frequency-domain impedance curve by filling in the missing values is not a trivial exercise due to the influence of this choice on the IR. We recommend using a physical model as much as possible, potentially by first making use of an inverse identification procedure to evaluate unknown physical properties, i.e., the intrinsic parameters of a foam (porosity, tortuosity, etc.). Such methods are now routinely used with impedance tube measurements [68–70]. Another potential strategy would be to attempt the direct identification of the IR of a given material in the time domain using short bursts.

Continuity of the impedance operator, or in this case of the reflection coefficient, is not required for the FT to be meaningful. However, one should expect a Gibbs phenomenon in that case, so it is recommended to smoothly transition whenever possible.

As an additional benefit of its intrinsic broadband aspect, the IR–TDIBC ensures the passivity property on the entire frequency spectrum of the simulation, including the smallest wavelengths which are associated to spurious noise. This ensures that such noise is properly filtered by the TDIBC and never amplified.

6.2 On the numerical cost

One of the advantages of the IR–TDIBC approach is that the associated numerical burden is quite low: in the linear case, one only needs summing arrays and "roll" them by one at every time step. In most of the situations encountered by the authors, the simulation time overhead was less than 1%.

When the non-linear case is considered, the call to the IR–TDIBC solver becomes more involved since an iFT is required to recalculate the IR. The default would be to re-evaluate the iFT of the reflection coefficient at each time step, as the value of the normal velocity changes with time. This is an unnecessary and resource-intensive task, since these iFTs are repeated needlessly. Indeed, we claim that the IR is a smoothly varying function of the normal velocity, and that one can thus also interpolate the non-linear impulse response $\boldsymbol{R}$ as a function of the normal velocity. One should then tabulate in advance the impulse response, and at each time step evaluate $\boldsymbol{R}$ by a linear or quadratic interpolation. While we have not yet implemented a non-linear version of the OD–TDIBC in the JAGUAR solver (following for instance Diab et al. [30]), adding the non-linear contribution would not drastically slow down the simulation compared with the linear case. The reason is that one only has to interpolate the parameters as a function of the normal velocity, and continue the simulation with these values.

Another avenue of research regarding simulation speed-up would be to consider using the TDIBC sparsely in time, since the simulation time step dt is usually exceedingly lower than the one required for acoustic analyses. One could thus consider an asynchronous TDIBC, for instance by saving an incremental variable using a moving average of the input and calling the TDIBC solver every m^{th} iteration. While this technique applies to most types of ADE-TDIBCs, it has an additional benefit in the case of the IR–TDIBC. By artificially increasing the dt of the IR–TDIBC, one reduces the frequency step Δf of the reflection coefficient represented by the IR. This is caused by the time-frequency relationship

$$\mathrm{dt}\Delta f = \mathrm{cst}, \tag{29}$$

meaning that for a given size of $\boldsymbol{R}$ on disk, one improves the frequency resolution by artificially increasing the time-step at the price of reducing the maximum frequency that can be resolved by the TDIBC. This drawback is not problematic since the time-step of the TDIBC can be selected a priori to match the expected frequency content of the signals (or 20 kHz by default in aeroacoustic problems).

Of the above methods (interpolation and asynchronization), only the former was implemented in the JAGUAR solver.

6.3 On the memory cost

One of the historical reasons why the IR–TDIBC was not introduced earlier is certainly the additional memory cost associated with storing the future response of the TDIBC, i.e. the $\boldsymbol{y}_N$ array in Eq. 17. This array needs to be saved at each degree of freedom located at the TDIBC, and its size N_R depends on the size of the FFT. This size is selected explicitly by the user to obtain a given frequency resolution of the reflection coefficient, which also depends on the TDIBC time-step dt (which can be, as explained above, greater than the simulation dt). A striking feature of the IR–TDIBC is that its cost in memory (and simulation time) is not controlled by the maximum frequency resolved in the simulation. This behavior is dissimilar to what happens with the ADE–TDIBC family, where the number of parameters depends on the frequency range of interest. The process of finding these parameters has to be done prior to the simulation, and sometimes involves solving a non-linear optimization problem of high dimension. These parameters lead to additional variables that have to be advected on a 1D mesh that is tailored to the simulation, thus requiring additional memory space. The OD–TDIBC approach is, in our experience, much less memory-demanding than the IR–TDIBC proposed in this work. A fair comparison between the two methods remains difficult since they have different limitations, but a factor of one or two orders of magnitude is observed in terms of *additional* memory usage by the IR–TDIBC. Note that in practice, this additional memory usage remains small compared with the memory available in current machines, due to TDIBCs being a boundary problem with few DoFs compared with the rest of the domain. This comparison is more favorable in 3D than in 2D, but even in the 2D cases treated in the present work, the memory overhead was negligible.

6.4 On the representativeness and utility of the IR–TDIBC approach

One noteworthy advantage of the IR-TDIBC is its remarkable ability to efficiently represent various types of liners, requiring minimal effort on the part of the user. While the ADE–TDIBC class of methods involves the (sometimes complex) optimization of parameters to fit a model or experimental data, the IR–TDIBC only relies on the iFT. Starting from an experimentally obtained impedance curve, one first has to extend the data with values from 0 Hz up to the maximum frequency 1/dt required during the iFT calculation of the impulse response in Eq. 9. Using the classical models from the literature, such as the one in Eq. 3, one can indicate values for the reflection coefficient that remain consistent with the physics.

6.5 Using the python script

To accompany the present paper and to disseminate our approach to the community, a python script is given alongside for educational purposes. To run the script, python 3 is required, along with the numpy and matplotlib libraries. With *linear_IR_ TDIBC.py*, the reader will get familiar with the linear case and reproduce the results of Figs. 4–6.

7 Conclusions

The last decades of efforts in representing aeroacoustic liners in the time domain have focused on incorporating additional variables to capture the complex oscillatory-diffusive behaviors occurring within the liners. The present work reintroduces an alternative approach based on the impulse response of the reflection coefficient and extends it to non-linear cases. The IR can be obtained by using an iFT, and provides a complete picture of the future states of the waves reflected by the liner after being subjected to a Dirac impulse.

In numerical simulations, signals are treated as subsequent Dirac impulses of varying amplitudes, allowing for straightforward sequential treatment by a liner BC based on the impulse response. In the present work, the reflection coefficient (scattering operator) was favored to handle the wave characteristics due to its boundedness, as opposed to the surface impedance or admittance. This IR–TDIBC approach, which had been discarded in the past for memory cost reasons, can now be considered an affordable option given the power available in modern computers. The main contribution of this work is the introduction of a generic method to handle non-linear behaviors using the IR-TDIBC approach.

The proposed approach was validated against exact theoretical results for the linear case and tested against impedance tube experiments with non-linear SDoF liner samples displaying a non-linear behavior. A satisfactory agreement was observed between the experiments and the model. Furthermore, the propagation of waves in a 2D duct geometry was considered, and the Navier-Stokes equations were solved in a no-flow configuration representative of ducts used in impedance eduction. The authors confirmed, as was recently reported in the literature, that the impedance of such SDoF liners was a function of space due to the decrease of the SPL over the liner.

Some benefits of using the IR–TDIBC method are listed below:

1. **Parameter free approach**: there is no need to fit any parameter, one only has to calculate the impulse response of the reflection coefficient.
2. **Generalization**: the method can readily handle any type of impedance, such as that of a metasurface made of a parallel assembly of complex liners.
3. **Fast**: only a low additional numerical complexity is introduced by the IR–TDIBC approach, i.e., a sum of arrays.
4. **Ease of integration**: the proposed approach behaves as an input-output blackbox for any code written in an NSCBC formalism to impose the BCs, easing the coupling with existing flow solvers.

The authors have included a collection of Python scripts alongside the current work that may be of interest to the community that intends to begin working with the IR-TDIBC. The scripts can serve as a starting point for future research and ideally demonstrate the straightforward integration of the method, as well as its ability to accurately represent all types of liners and handle both continuous and discontinuous incident waves with ease. Further studies should concentrate on incorporating the method with implicit time schemes since it is currently limited to explicit time integration.

Acknowledgments

The authors would like to thank Estelle Piot, Florian Monteghetti and Hugues Deniau for the fruitful discussions that took place during the writing of this paper.

Data statement

The data that support the findings of this study are available from the corresponding author, R.R., upon reasonable request.

References

[1] G. Bielak, J. Gallman, R. Kunze, P. Murray, J. Premo, M. Kosanchick, A. Hersh, J. Celano, B. Walker, J. Yu, et al., Advanced nacelle acoustic lining concepts development, Tech. rep. (2002).
URL `https://core.ac.uk/download/pdf/42768488.pdf`

[2] U. Ingard, On the theory and design of acoustic resonators, The Journal of the acoustical society of America 25 (6) (1953) 1037–1061. `doi:10.1121/1.1907235`.

[3] C. K. Tam, K. A. Kurbatskii, K. Ahuja, R. Gaeta Jr, A numerical and experimental investigation of the dissipation mechanisms of resonant acoustic liners, Journal of Sound and Vibration 245 (3) (2001) 545–557. `doi:10.1006/jsvi.2001.3571`.

[4] L. L. Beranek, Acoustic impedance of porous materials, The Journal of the Acoustical Society of America 13 (3) (1942) 248–260. `doi:10.1121/1.1916172`.

[5] E. Brandão, P. Mareze, A. Lenzi, A. R. da Silva, Impedance measurement of non-locally reactive samples and the influence of the assumption of local reaction, The Journal of the Acoustical Society of America 133 (5) (2013) 2722–2731. `doi:10.1121/1.4799015`.

[6] L. Crocco, Research on combustion instability in liquid propellant rockets, in: Symposium (International) on Combustion, Vol. 12, Elsevier, 1969, pp. 85–99. `doi:10.1016/S0082-0784(69)80394-2`.

[7] R. J. Priem, E. J. Rice, Combustion instability with finite mach number flow and acoustic liners, in: Symposium (International) on Combustion, Vol. 12, Elsevier, 1969, pp. 149–159. `doi:10.1016/S0082-0784(69)80399-1`.

[8] C. Oberg, Combustion stabilization with acoustic cavities., Journal of Spacecraft and Rockets 8 (12) (1971) 1220–1225. `doi:10.2514/3.30366`.

[9] Q. Douasbin, C. Scalo, L. Selle, T. Poinsot, Delayed-time domain impedance boundary conditions (d-tdibc), Journal of Computational Physics 371 (2018) 50–66. `doi:10.1016/j.jcp.2018.05.003`.

[10] L. Sivian, Acoustic impedance of small orifices, The Journal of the Acoustical Society of America 7 (2) (1935) 94–101. `doi:10.1121/1.1915795`.

[11] U. Ingård, S. Labate, Acoustic circulation effects and the nonlinear impedance of orifices, The Journal of the Acoustical Society of America 22 (2) (1950) 211–218. `doi:10.1121/1.1906591`.

[12] C. Richter, J. A. Hay, N. Schönwald, S. Busse, F. Thiele, et al., A review of time-domain impedance modelling and applications, Journal of Sound and Vibration 330 (16) (2011) 3859–3873. `doi:10.1016/j.jsv.2011.04.013`.

[13] K. Yee, Numerical solution of initial boundary value problems involving maxwell's equations in isotropic media, IEEE Transactions on antennas and propagation 14 (3) (1966) 302–307. `doi:10.1109/TAP.1966.1138693`.

[14] R. J. Luebbers, F. Hunsberger, Fdtd for nth-order dispersive media, IEEE transactions on Antennas and Propagation 40 (11) (1992) 1297–1301. `doi:10.1109/8.202707`.

[15] R. Luebbers, F. P. Hunsberger, K. S. Kunz, R. B. Standler, M. Schneider, A frequency-dependent finite-difference time-domain formulation for dispersive materials, IEEE Transactions on Electromagnetic Compatibility 32 (3) (1990) 222–227. `doi:10.1109/15.57116`.

[16] Y. Reymen, M. Baelmans, W. Desmet, Efficient implementation of tam and auriault's time-domain impedance boundary condition, AIAA journal 46 (9) (2008) 2368–2376. `doi:10.2514/1.35876`.

[17] C. K. Tam, L. Auriault, Time-domain impedance boundary conditions for computational aeroacoustics, AIAA journal 34 (5) (1996) 917–923. `doi:10.2514/3.13168`.

[18] Y. Özyörük, L. N. Long, M. G. Jones, Time-domain numerical simulation of a flow-impedance tube, Journal of Computational Physics 146 (1) (1998) 29–57. `doi:10.1006/jcph.1998.5919`.

[19] D. M. Sullivan, Frequency-dependent fdtd methods using z transforms, IEEE Transactions on Antennas and Propagation 40 (10) (1992) 1223–1230. `doi:10.1109/8.182455`.

[20] D. M. Sullivan, Z-transform theory and the fdtd method, IEEE Transactions on Antennas and Propagation 44 (1) (1996) 28–34. `doi:10.1109/8.477525`.

[21] M. Myers, On the acoustic boundary condition in the presence of flow, Journal of Sound and Vibration 71 (3) (1980) 429–434. `doi:10.1016/0022-460X(80)90424-1`.

[22] S. Rienstra, Impedance models in time domain, including the extended helmholtz resonator model, in: 12th AIAA/CEAS Aeroacoustics Conference (27th AIAA Aeroacoustics Conference), 2006, p. 2686. `doi:10.2514/6.2006-2686`.

[23] S.-H. Ko, Sound attenuation in lined rectangular ducts with flow and its application to the reduction of aircraft engine noise, The Journal of the Acoustical Society of America 50 (6A) (1971) 1418–1432. `doi:10.1121/1.1912784`.

[24] J. D. Jackson, Classical electrodynamics, 2nd Edition, John Wiley & Sons, New-York, 1975.

[25] R. M. Joseph, S. C. Hagness, A. Taflove, Direct time integration of maxwell's equations in linear dispersive media with absorption for scattering and propagation of femtosecond electromagnetic pulses, Optics Letters 16 (18) (1991) 1412–1414. `doi:10.1364/OL.16.001412`.

[26] D. Dragna, P. Pineau, P. Blanc-Benon, A generalized recursive convolution method for time-domain propagation in porous media, The Journal of the Acoustical Society of America 138 (2) (2015) 1030–1042. `doi:10.1121/1.4927553`.

[27] F. Monteghetti, D. Matignon, E. Piot, L. Pascal, Design of broadband time-domain impedance boundary conditions using the oscillatory-diffusive representation of acoustical models, J. Acoust. Soc. Am. 140 (3) (2016) 1663–1674. `doi:10.1121/1.4962277`.

[28] F. Monteghetti, D. Matignon, E. Piot, Energy analysis and discretization of nonlinear impedance boundary conditions for the time-domain linearized euler equations, Journal of Computational Physics 375 (2018) 393–426. `doi:10.1016/j.jcp.2018.08.037`.

[29] R. Troian, D. Dragna, C. Bailly, M.-A. Galland, Broadband liner impedance eduction for multimodal acoustic propagation in the presence of a mean flow, Journal of Sound and Vibration 392 (2017) 200–216. `doi:10.1016/j.jsv.2016.10.014`.

[30] D. Diab, D. Dragna, E. Salze, M.-A. Galland, Nonlinear broadband time-domain admittance boundary condition for duct acoustics. application to perforated plate liners, Journal of Sound and Vibration 528 (2022) 116892. `doi:10.1016/j.jsv.2022.116892`.

[31] Y. Liu, M. Vinokur, Z. J. Wang, Spectral difference method for unstructured grids i: Basic formulation, Journal of Computational Physics 216 (2) (2006) 780–801. `doi:10.1016/j.jcp.2006.01.024`.

[32] M. Dumbser, C.-D. Munz, Ader discontinuous galerkin schemes for aeroacoustics, Comptes Rendus Mécanique 333 (9) (2005) 683–687. `doi:10.1016/j.crme.2005.07.008`.

[33] B. Cockburn, G. E. Karniadakis, C.-W. Shu, Discontinuous Galerkin methods: theory, computation and applications, Vol. 11, Springer Science & Business Media, Berlin, 2012. `doi:10.1007/979-3-642-59721-3`.

[34] T. J. Poinsot, S. Lelef, Boundary conditions for direct simulations of compressible viscous flows, Journal of computational physics 101 (1) (1992) 104–129. `doi:10.1016/0021-9991(92)90046-2`.

[35] R. Fiévet, H. Deniau, E. Piot, Strong compact formalism for characteristic boundary conditions with discontinuous spectral methods, Journal of Computational Physics 408 (2020) 109276. `doi:10.1016/j.jcp.2020.109276`.
URL `https://www.sciencedirect.com/science/article/pii/S0021999120300504`

[36] L. Casadei, T. Node-Langlois, H. Deniau, E. Piot, C. Polacsek, Towards sound absorption in a cylindrical lined duct using cfd with time-domain impedance boundary condition, in: AIAA Aviation 2021 Forum, 2021, p. 2297. `doi:10.2514/6.2021-2297`.

[37] L. Casadei, Time-domain broadband impedance model for computational aeroacoustics: application to shock-wave propagation in lined intakes, Ph.D. thesis, Toulouse, ISAE (2022).

[38] M. G. Jones, F. Simon, R. Roncen, Broadband and low-frequency acoustic liner investigations at nasa and onera, AIAA Journal 60 (4) (2022) 2481–2500. `doi:10.2514/1.J060862`.

[39] A. H. Nayfeh, J. E. Kaiser, D. P. Telionis, Acoustics of aircraft engine-duct systems, Aiaa Journal 13 (2) (1975) 130–153. `doi:10.2514/3.49654`.

[40] A. B. Bauer, Impedance theory and measurements on porous acoustic liners, Journal of Aircraft 14 (8) (1977) 720–728. `doi:10.2514/3.58844`.

[41] N. Atalla, F. Sgard, Modeling of perforated plates and screens using rigid frame porous models, Journal of sound and vibration 303 (1-2) (2007) 195–208. `doi:10.1016/j.jsv.2007.01.012`.

[42] Y. Ventribout, Contrôle des perturbations aéroacoustiques par impédances de parois: application à un modèle de matériaux poreux, Ph.D. thesis, Ecole nationale superieure de l'aeronautique et de l'espace (2006).

[43] J. Allard, N. Atalla, Propagation of Sound in Porous Media: Modelling Sound Absorbing Materials 2e, John Wiley & Sons, New York, 2009. `doi:10.1002/9780470747339`.

[44] M. Bruneau, Fundamentals of acoustics, London, UK, 2006.

[45] R. L. Panton, A. L. Goldman, Correlation of nonlinear orifice impedance, The Journal of the Acoustical Society of America 60 (6) (1976) 1390–1396. `doi:10.1121/1.381232`.

[46] T. H. Melling, The acoustic impendance of perforates at medium and high sound pressure levels, J. Sound Vib. 29 (1) (1973) 1–65. `doi:10.1016/S0022-460X(73)80125-7`.

[47] A. Guess, Calculation of perforated plate liner parameters from specified acoustic resistance and reactance, J. Sound Vib. 40 (1) (1975) 119–137. `doi:10.1016/S0022-460X(75)80234-3`.

[48] R. Billard, G. Gabard, M. Versaevel, G. Tissot, A non-linear impedance model for micro-perforated liners, in: e-Forum Acusticum 2020, 2020.
URL `https://hal.inria.fr/hal-03143278/document`

[49] B. M. Howerton, H. Vold, M. G. Jones, Application of swept sine excitation for acoustic impedance eduction, in: 25th AIAA/CEAS Aeroacoustics Conference, 2019, p. 2487. `doi:10.2514/6.2019-2487`.

[50] J. G. Leishman, Challenges in modeling the unsteady aerodynamics of wind turbines, in: Wind Energy Symposium, Vol. 7476, 2002, pp. 141–167. `doi:10.1115/WIND2002-37`.

[51] M. J. Kemp, Analysis and simulation of non-linear audio processes using finite impulse responses derived at multiple impulse amplitudes, in: Audio Engineering Society Convention 106, Audio Engineering Society, 1999.

[52] A. Farina, E. Armelloni, Emulation of not-linear, time-variant devices by the convolution technique, in: Congresso AES Italia, Como, 2005.

[53] J. Blank, K. Deb, Pymoo: Multi-objective optimization in python, IEEE Access 8 (2020) 89497–89509.

[54] D. L. Johnson, J. Koplik, R. Dashen, Theory of dynamic permeability and tortuosity in fluid-saturated porous media, J. Fluid Mech. 176 (1987) 379–402. `doi:10.1017/S0022112087000727`.

[55] Y. Champoux, J.-F. Allard, Dynamic tortuosity and bulk modulus in air-saturated porous media, J. Appl. Acoust. 70 (4) (1991) 1975–1979. `doi:10.1063/1.349482`.

[56] R. Roncen, P. Vuillemin, P. Klotz, F. Simon, F. Méry, D. Sebbane, E. Piot, Design and optimization of acoustic liners with a shear grazing flow: Opal software platform applications, in: INTER-NOISE and NOISE-CON Congress and Conference Proceedings, Vol. 263, Institute of Noise Control Engineering, 2021, pp. 152–163. `doi:10.3397/IN-2021-1308`.

[57] K. V. Horoshenkov, A. Khan, F.-X. Bécot, L. Jaouen, F. Sgard, A. Renault, N. Amirouche, F. Pompoli, N. Prodi, P. Bonfiglio, et al., Reproducibility experiments on measuring acoustical properties of rigid-frame porous media (round-robin tests), The Journal of the Acoustical Society of America 122 (1) (2007) 345–353. `doi:10.1121/1.2739806`.

[58] American Society of Mechanical Engineers Digital Collection, Comparison of various CFD codes for LES simulations of turbomachinery: from inviscid vortex convection to multi-stage compressor, Vol. 2C: Turbomachinery.

[59] A. Cassagne, J. Boussuge, N. Villedieu, G. Puigt, I. D'ast, A. Genot, Jaguar: a new CFD code dedicated to massively parallel high-order LES computations on complex geometry, in: The 50th 3AF International Conference on Applied Aerodynamics (AERO 2015), 2015.

[60] K. Van den Abeele, C. Lacor, Z. Wang, On the stability and accuracy of the spectral difference method, Journal of Scientific Computing 37 (2) (2008) 162–188.

[61] A. Jameson, A proof of the stability of the spectral difference method for all orders of accuracy, Journal of Scientific Computing 45 (1-3) (2010) 348–358.

[62] D. Kopriva, A staggered-grid multidomain spectral method for the compressible navier–stokes equations, Journal of Computational Physics 143 (1) (1998) 125–158.

[63] J. Berland, C. Bogey, C. Bailly, Low-dissipation and low-dispersion fourth-order Runge–Kutta algorithm, Computers & Fluids 35 (10) (2006) 1459–1463.

[64] J. W. Kim, D. J. Lee, Generalized characteristic boundary conditions for computational aeroacoustics, AIAA journal 38 (11) (2000) 2040–2049.

[65] R. Roncen, F. Méry, E. Piot, P. Klotz, Spatially-varying impedance model for locally reacting acoustic liners at a high sound intensity, Journal of Sound and Vibration 524 (2022) 116741. `doi:10.1016/j.jsv.2021.116741`.

[66] V. Lafont, F. Méry, R. Roncen, F. Simon, E. Piot, Liner impedance eduction under shear grazing flow at a high sound pressure level, AIAA Journal 58 (3) (2020) 1107–1117. `doi:10.2514/1.J058756`.

[67] C. E. Shannon, Communication in the presence of noise, Proceedings of the IRE 37 (1) (1949) 10–21. `doi:10.1109/JRPROC.1949.232969`.

[68] J.-D. Chazot, E. Zhang, J. Antoni, Acoustical and mechanical characterization of poroelastic materials using a bayesian approach, J. Acoust. Soc. Am. 131 (6) (2012) 4584–4595. `doi:10.1121/1.3699236`.

[69] T. G. Zieliński, Normalized inverse characterization of sound absorbing rigid porous media, J. Acoust. Soc. Am. 137 (6) (2015) 3232–3243. `doi:10.1121/1.4919806`.

[70] R. Roncen, Z. E. A. Fellah, E. Ogam, Addressing the ill-posedness of multi-layer porous media characterization in impedance tubes through the addition of air gaps behind the sample: numerical validation, Journal of Sound and Vibration 520 (2022) 116601. `doi:10.1016/j.jsv.2021.116601`.